

## Large-scale chemical evolution of the Arctic vortex during the 1999/2000 winter: HALOE/POAM III Lagrangian photochemical modeling for the SAGE III—Ozone Loss and Validation Experiment (SOLVE) campaign

R. B. Pierce,<sup>1</sup> J. Al-Saadi,<sup>1</sup> T. D. Fairlie,<sup>1</sup> M. Natarajan,<sup>1</sup> V. L. Harvey,<sup>2</sup> W. L. Grose,<sup>1</sup> J. M. Russell III,<sup>3</sup> R. Bevilacqua,<sup>4</sup> S. D. Eckermann,<sup>4</sup> D. Fahey,<sup>5</sup> P. Popp,<sup>5</sup> E. Richard,<sup>5</sup> R. Stimpfle,<sup>6</sup> G. C. Toon,<sup>7</sup> C. R. Webster,<sup>7</sup> and J. Elkins<sup>8</sup>

Received 3 July 2001; revised 20 December 2002; accepted 1 March 2002; published 18 December 2002.

[1] The LaRC Lagrangian Chemical Transport Model (LaRC LCTM) is used to simulate the kinematic and chemical evolution of an ensemble of trajectories initialized from Halogen Occultation Experiment (HALOE) and Polar Ozone and Aerosol Measurement (POAM) III atmospheric soundings over the SAGE III—Ozone Loss and Validation Experiment (SOLVE) campaign period. Initial mixing ratios of species which are not measured by HALOE or POAM III are specified using sunrise and sunset constituent CH<sub>4</sub> and constituent PV regressions obtained from the LaRC IMPACT model, a global three dimensional general circulation and photochemical model. Ensemble averaging of the trajectory chemical characteristics provides a vortex-average perspective of the photochemical state of the Arctic vortex. The vortex-averaged evolution of ozone, chlorine, nitrogen species, and ozone photochemical loss rates is presented. Enhanced chlorine catalyzed ozone loss begins in mid-January above 500 K, and the altitude of the peak loss gradually descends during the rest of the simulation. Peak vortex averaged loss rates of over 60 ppbv/day occur in early March at 450 K. Vortex averaged loss rates decline after mid-March. The accumulated photochemical ozone loss during the period from 1 December 1999 to 30 March 2000 peaks at 450 K with net losses of near 2.2 ppmv. The predicted distributions of CH<sub>4</sub>, O<sub>3</sub>, denitrification, and chlorine activation are compared to the distributions obtained from in situ measurements to evaluate the accuracy of the simulations. The comparisons show best agreement when diffusive tendencies are included in the model calculations, highlighting the importance of this process in the Arctic vortex. Sensitivity tests examining the large-scale influence of orographically generated gravity-wave temperature anomalies are also presented. Results from this sensitivity study show that mountain-wave temperature perturbations contribute an additional 2–8% O<sub>3</sub> loss during the 1999/2000 winter.

**INDEX TERMS:** 0341 Atmospheric Composition and Structure: Middle atmosphere—constituent transport and chemistry (3334); 3360 Meteorology and Atmospheric Dynamics: Remote sensing; 3334 Meteorology and Atmospheric Dynamics: Middle atmosphere dynamics (0341, 0342); **KEYWORDS:** photochemical, Lagrangian, Arctic, ozone, HALOE, POAM, SOLVE

**Citation:** Pierce, R. B., et al., Large-scale chemical evolution of the Arctic vortex during the 1999/2000 winter: HALOE/POAM III Lagrangian photochemical modeling for the SAGE III—Ozone Loss and Validation Experiment (SOLVE) campaign, *J. Geophys. Res.*, 107, 8317, doi:10.1029/2001JD001063, 2002. [printed 108(D5), 2003]

<sup>1</sup>NASA Langley Research Center, Hampton, Virginia, USA.

<sup>2</sup>Science Applications International Corporation, Hampton, Virginia, USA.

<sup>3</sup>Center for Atmospheric Sciences, Hampton University, Hampton, Virginia, USA.

<sup>4</sup>Naval Research Laboratory, Washington, D.C., USA.

<sup>5</sup>Aeronomy Laboratory, NOAA, Boulder, Colorado, USA.

<sup>6</sup>Department of Earth and Planetary Science, Harvard University, Cambridge, Massachusetts, USA.

<sup>7</sup>NASA Jet Propulsion Laboratory, Pasadena, California, USA.

<sup>8</sup>NOAA/Climate Monitoring and Diagnostic Laboratory, Boulder, Colorado, USA.

### 1. Introduction

[2] Arctic springtime ozone loss has been observed for a number of years [e.g., McKenna *et al.*, 1990; Salawitch *et al.*, 1990; Hoffman and Deshler, 1991; Proffitt *et al.*, 1993] although the total reduction in column ozone amounts has typically been much less than for the Antarctic region. The absence of extensive Northern Hemisphere ozone depletion is primarily due to the more transient nature of the Arctic vortex, which tends to experience some degree of disruption over the course of the winter, leading to warmer temperatures, and less persistent polar stratospheric cloud (PSC) decks. The lack of persistent PSCs means that the denitri-

# Report Documentation Page

Form Approved  
OMB No. 0704-0188

Public reporting burden for the collection of information is estimated to average 1 hour per response, including the time for reviewing instructions, searching existing data sources, gathering and maintaining the data needed, and completing and reviewing the collection of information. Send comments regarding this burden estimate or any other aspect of this collection of information, including suggestions for reducing this burden, to Washington Headquarters Services, Directorate for Information Operations and Reports, 1215 Jefferson Davis Highway, Suite 1204, Arlington VA 22202-4302. Respondents should be aware that notwithstanding any other provision of law, no person shall be subject to a penalty for failing to comply with a collection of information if it does not display a currently valid OMB control number.

1. REPORT DATE <b>20 DEC 2002</b>		2. REPORT TYPE		3. DATES COVERED <b>00-00-2002 to 00-00-2002</b>	
4. TITLE AND SUBTITLE <b>Large-scale chemical evolution of the Arctic vortex during the 1999/2000 winter: HALOE/POAM III Lagrangian photochemical modeling for the SAGE III - Ozone Loss and Validation Experiment (SOLVE) campaign</b>				5a. CONTRACT NUMBER	
				5b. GRANT NUMBER	
				5c. PROGRAM ELEMENT NUMBER	
6. AUTHOR(S)				5d. PROJECT NUMBER	
				5e. TASK NUMBER	
				5f. WORK UNIT NUMBER	
7. PERFORMING ORGANIZATION NAME(S) AND ADDRESS(ES) <b>Naval Research Laboratory, E.O. Hulburt Center for Space Research, Washington, DC, 20375</b>				8. PERFORMING ORGANIZATION REPORT NUMBER	
9. SPONSORING/MONITORING AGENCY NAME(S) AND ADDRESS(ES)				10. SPONSOR/MONITOR'S ACRONYM(S)	
				11. SPONSOR/MONITOR'S REPORT NUMBER(S)	
12. DISTRIBUTION/AVAILABILITY STATEMENT <b>Approved for public release; distribution unlimited</b>					
13. SUPPLEMENTARY NOTES					
14. ABSTRACT					
15. SUBJECT TERMS					
16. SECURITY CLASSIFICATION OF:			17. LIMITATION OF ABSTRACT <b>Same as Report (SAR)</b>	18. NUMBER OF PAGES <b>26</b>	19a. NAME OF RESPONSIBLE PERSON
a. REPORT <b>unclassified</b>	b. ABSTRACT <b>unclassified</b>	c. THIS PAGE <b>unclassified</b>			

fication necessary for maintaining high levels of chlorine activation required for significant spring time chlorine-catalyzed ozone destruction is often not realized in the Arctic [Solomon, 1999]. However, long-term observations of total ozone by the Total Ozone Mapping Spectrometer (TOMS) indicate significant declines in total ozone over the Arctic during the last decade [Newman *et al.*, 1997]. Column ozone losses in the lower stratosphere of as much as 50% of the column above the 150 hPa level have been calculated by Müller *et al.* [1996] using coincident measurements of O<sub>3</sub> and CH<sub>4</sub> by HALOE. The potential severity of Arctic ozone loss was made quite evident during 1997, when an anomalously persistent vortex resulted in record low ozone. In contrast, the 1998 boreal winter showed warmer vortex temperatures and more normal springtime column ozone amounts [Schultz *et al.*, 2001].

[3] The wide variability in Northern Hemisphere springtime ozone amounts is due to a strong coupling between chlorine loading and planetary-wave dynamics. Interannual variability in the Northern Hemisphere circulation leads to significant long-term variability in Arctic temperatures, ozone transport and photochemistry. Episodic planetary-wave disturbances lead to significant intraseasonal ozone transport and photochemical variability within the Arctic. The transient nature of the Arctic vortex also means that variations in vertical transport and diffusive mixing processes tend to play a more important role in determining the distribution of column ozone in the Arctic than in the Antarctic, where the vortex is more isolated and stable. This transience, coupled with wide variations in the extent of denitrification and chlorine activation, tends to complicate the observationally based determination of the chemical loss within the Arctic vortex.

[4] The 1999/2000 winter presents a unique opportunity to test our understanding of Arctic ozone loss because the extent and duration of the Arctic cold pool was one of the largest, and longest on record [Manney and Sabutis, 2000] therefore significant denitrification and chlorine activation should have occurred. Furthermore, the large amount of in situ, remote, and balloon data available from the SAGE III Ozone Loss and Validation Experiment (SOLVE) Campaign, which was conducted during November–March 1999/2000, provides an unprecedented opportunity to test our theoretical understanding of Arctic ozone loss processes.

[5] The LaRC Lagrangian Chemical Transport Model (LaRC LCTM) [Pierce *et al.*, 1996, 1999] was used during the 1999/2000 SOLVE campaign to provide real-time forecasts of the hemispheric distribution of catalytic ozone loss processes, transport, and mixing in the lower and middle stratosphere. The model uses daily satellite observations of ozone and other key species from the Halogen Occultation Experiment (HALOE) [Russell *et al.*, 1993] and the Polar Ozone and Aerosol Measurement (POAM III) [Lucke *et al.*, 1999] to initialize an ensemble of trajectories. The LaRC LCTM then predicts the photochemical, microphysical, and diffusive tendencies along these trajectories. The number of trajectories increases as the integration proceeds, resulting in an ensemble Lagrangian prediction of the chemical and microphysical state of the Arctic stratosphere. The SOLVE LaRC LCTM predictions provide a large-scale perspective of ozone loss and transport processes to aid in the inter-

pretation of in situ and remote data collected during the SOLVE field campaign. Satellite solar occultation measurements, in conjunction with the LaRC LCTM, significantly enhance the vertical and longitudinal extent of the observational and theoretical database for SOLVE and allow us to examine the relative contributions of advective, diffusive, and photochemical processes in determining the observed evolution of ozone within the Arctic vortex.

[6] The format of this paper is as follows. We begin with a discussion of recent modifications to the model which were needed to properly simulate the Arctic stratosphere and a description of the SOLVE simulation. Then we present a discussion of the vortex-averaged evolution of the simulation over the course of the 1999/2000 winter. Next we present comparisons of the model results with in situ observations from instruments onboard the ER2, examine two specific case studies in detail, and summarize the integrated budgets of O<sub>3</sub> and NO<sub>y</sub> within the Arctic vortex. Finally, we present a sensitivity study that explores the impact of orographically generated gravity-wave temperature perturbations on the vortex O<sub>3</sub> and NO<sub>y</sub> budgets.

## 2. The LaRC Lagrangian Chemical Transport Model (LaRC LCTM)

[7] The LaRC LCTM is formulated in isentropic coordinates and uses once daily 12Z winds and temperatures obtained from the United Kingdom Meteorological Office (UKMO) Upper Atmospheric Research Satellite (UARS) assimilation [Swinbank and O'Neill, 1994]. The horizontal resolution of the UKMO data is 3.75° in longitude by 2.5° in latitude and has 18 pressure levels from the surface to 0.4hPa. The vertical resolution is 5 pressure levels per decade that are uniform in log pressure (approximately 3km resolution). Assimilated winds and temperatures are interpolated to 34 isentropic surfaces extending from 240K to 400K by 10K, 400K to 550K by 25K, 600K to 1000K by 100K, and 1000K to 2000K by 200K increments. This gives a nominal vertical resolution for the trajectory calculations of approximately 1.0 km in the lower stratosphere.

[8] The UKMO assimilated temperatures and the MID-RAD radiative code [Shine, 1987] are used to compute radiative heating rates ( $R_{\text{total}}$ ), which are used to determine the vertical displacement of the trajectories. Mass conservation is assured by adjusting the short-wave component of the radiative heating ( $R_{\text{shortwave}}$ ) such that the globally averaged radiative heating rate on a pressure surface is zero. The adjustment ( $1. - R_{\text{total}}/R_{\text{shortwave}}$ ) scales the shortwave component of the heating and leaves the long-wave component of the heating unmodified. This adjustment procedure was chosen since it tends to maintain the strong radiative cooling found in the Arctic vortex during polar night much better than a global adjustment of the total heating rate and results in better predictions of the vertical profiles of long-lived species with strong vertical gradients (such as N<sub>2</sub>O and CH<sub>4</sub>) in the Arctic vortex.

[9] The isentropic data base for the model also includes daily, 3D distributions of winds, temperatures, potential vorticity,  $Q$  [Fairlie *et al.*, 1999], a measure of the relative strength of strain and rotation in the flow, stream function, velocity potential, overhead column ozone, and a circulation flag which identifies the polar vortex (regions where  $Q$  is

negative and vorticity is positive when integrated along streamlines defined by the rotational component of the flow) as well as the location of closed anticyclonic circulations (regions where  $Q$  is negative and vorticity is negative when integrated along rotational streamlines). The overhead column ozone is used for the model photolysis rates and is determined from PV- $\theta$  mapped ozone distributions that combine information from HALOE, SAGE II, and POAM III ozone profiles observed during SOLVE. Separate PV- $O_3$  regressions are obtained by binning the satellite measurements in PV bins on each isentropic level for 3 distinct  $Q$  based circulation types (vortex, anticyclone, or neither) for both Northern and Southern Hemispheres, and 3 different time periods (October–November 1999, December–January 2000, and February–March 2000). Comparison of the PV- $\theta$  mapped column  $O_3$  with TOMS shows good agreement in the daily evolution of the large-scale features although the PV- $\theta$  mapped column is lower than TOMS in regions with particularly high column ozone. This is likely due to the fact that very few of the satellite measurements go below 400K–425K and so the ozone column in the lower most stratosphere is missed. Comparisons with other PV- $\theta$  mapped  $O_3$  products [Randall *et al.*, 2002] shows very good quantitative agreement.

[10] The chemical module of the LaRC LCTM is from the NASA Langley Interactive Modeling project for Atmospheric Chemistry and Transport (IMPACT) model [Al-Saadi *et al.*, 2002; Pierce *et al.*, 2000; Eckman *et al.*, 1995], which is a coupled 3D chemical-dynamical model of the troposphere and stratosphere. The implementation of the chemical module in the LaRC LCTM is described by Pierce *et al.* [1999] and recent developments are described here.

[11] The representation of stratospheric heterogeneous chemical processes and tropospheric chemistry have been updated, allowing us to further improve agreement of modeled ozone with observations in the troposphere and lower stratosphere. With these changes, 35 chemical families and individual species are explicitly transported. A total of 53 chemical species are followed using 41 photolytic reactions and 101 gas-phase reactions. Concentrations of species not transported are obtained by partitioning of the chemical families using standard photochemical equilibrium techniques. The parameterization of heterogeneous processing has been improved by considering a more comprehensive reaction set and by using the analytical scheme of Carslaw *et al.* [1995] to determine the sulfate aerosol composition and effective reaction rates. Nine heterogeneous reactions, involving  $N_2O_5$ , chlorine, and bromine species, are now considered on both liquid aerosol and polar stratospheric cloud surfaces. Denitrification is parameterized as sedimentation of  $HNO_3$  in PSC particles in a manner similar to Chipperfield [1999]. The amount of condensed-phase  $HNO_3$  is determined through equilibrium relationships with the presence of condensed-phase  $HNO_3$  is taken as an indicator of type I PSCs, with an associated weak removal time constant of 25 days; the presence of condensed-phase  $H_2O$  is taken as an indicator of type II PSCs, with a much faster removal time constant of 2/3 day. These time constants are derived assuming mean fall velocities of 0.04 km/day and 1.5 km/day for the nominal 1.0 km vertical resolution of the isentropic database. These fall

velocities are appropriate for particles with 1.0–2.0 and 20.0 micron diameters, respectively [Toon *et al.*, 1989]. When type II PSCs are present, the local vapor-phase  $H_2O$  concentration is reduced accordingly, and dehydration through sedimentation is represented using the 2/3 day removal time constant.

[12] Accounting for an exchange of condensed-phase  $HNO_3$  and  $H_2O$  between trajectories through sedimentation and evaporation presents some unique challenges within the Lagrangian framework of the LaRC LCTM. Vertical exchange of condensed  $HNO_3$  and  $H_2O$  is evaluated by determining the average amount of condensed  $HNO_3$  or  $H_2O$  which has sedimented from trajectories above into each model gridbox (defined by the horizontal and vertical resolution of our isentropic meteorological fields) and then adding this amount to the gas-phase  $HNO_3$  and  $H_2O$  concentrations of all trajectories within that grid box. New condensed-phase  $HNO_3$  and  $H_2O$  concentrations are then evaluated for each trajectory within the grid box using equilibrium relationships, followed by sedimentation of any new condensed  $HNO_3$  or  $H_2O$  into the next vertical grid box. This sequential procedure accounts for sedimentation through multiple isentropic layers and vertical redistribution of condensed-phase  $HNO_3$  and  $H_2O$ .

[13] The LaRC LCTM is initialized using  $O_3$ ,  $H_2O$ ,  $NO_x$  ( $NO + NO_2$ ),  $CH_4$ ,  $HCl$ ,  $HF$ , and aerosol surface area density (SAD) observations from HALOE and  $O_3$ ,  $H_2O$ , and SAD observations from POAM III. Species considered in the model but not observed from the satellites, termed auxiliary species, are initialized using the IMPACT model climatology. Auxiliary HALOE species are initialized using HALOE  $CH_4$  and sunrise and sunset regressions between the auxiliary species and  $CH_4$  obtained from the IMPACT model climatology. Auxiliary POAM III species are obtained using UKMO PV (at the POAM III sounding) and a sunrise or sunset regression between the auxiliary species and PV from the IMPACT model climatology. Only those HALOE observations north of  $30^\circ S$  with less than 30% measurement uncertainty for  $O_3$ ,  $CH_4$ ,  $HF$ ,  $H_2O$ ,  $HCl$ , and Northern Hemisphere POAM III observations with less than 30% measurement uncertainty for  $O_3$  and  $H_2O$  are included in the simulations. The  $Cl_y$  is adjusted when the sum of the observed  $HCl$  and auxiliary  $CLNO_3 + HOCl$  is greater than the auxiliary  $Cl_y$  and the observed  $NO$  and  $NO_2$  are adjusted so that the sum of the  $NO_y$  species does not exceed the auxiliary  $NO_y$ . Initialization concludes with a 5-day diurnal adjustment in which HALOE  $O_3$ ,  $H_2O$ , and  $HCl$  and POAM III  $O_3$  and  $H_2O$  are reset to their initial values after each time step. This final initialization step reduces the large initial radical tendencies associated with chemical imbalances between the observations and IMPACT climatology.

[14] A Lagrangian parameterization of diffusive mixing is also included in the LaRC LCTM. This parameterization is based on n-member mixing concepts and has a mixing efficiency factor that is a function of the relative strength of strain and rotation in the flow ( $Q$ ) [Fairlie *et al.*, 1999]. Trajectories within regions of predominantly rotational flow have negative  $Q$  and mix with neighboring trajectories on a weak background mixing timescale of 60 days. Trajectories within regions of shear have positive  $Q$  and the mixing timescales can be as fast as 1–2 days under strong shear

deformation. The flow dependent diffusion results in episodic enhancements in mixing efficiencies for a particular trajectory as it moves in and out of shear zones. Sensitivity tests have shown that the mixing parameterization performs well in both strong and weak mixing regimes. See *Fairlie et al.* [1999] for a complete discussion of the physical basis for the diffusion parameterization.

[15] The time constants for mixing are the same as given by *Fairlie et al.* [1999]. However, the original formulation was found to be globally nonconservative. The nonconservation arose from two assumptions that changed the mean mixing ratio of the trajectories (n-members) involved in each mixing event. First, mixing tendencies were evaluated using different efficiencies for each trajectory, resulting in more rapid approach toward the n-member mean for some trajectories than others and changes in the n-member mean. Second, a fixed radius was used to determine the n-members involved in mixing with each trajectory. Consequently, a particular trajectory could be involved in more than 1 n-member mixing event (overlap), resulting in changes in the combined n-member mean. To assure global conservation we now choose the n-member mixing ensemble based on the UKMO assimilation grid resolution (all trajectories within 1 vertical grid box, 2 north-south, and 2 east-west neighboring grid boxes mix), thus avoiding overlap. To assure conservation of the mean mixing ratio during each mixing event we now use a 9-point averaged Q from the UKMO grid to determine the mixing efficiency for all trajectories in the event. The new formulation results in episodic enhancements in the mean absolute amplitude of the diffusive tendencies within the Arctic vortex as internal shear zones develop in response to vortex deformation, but cannot instantaneously change the mean mixing ratio within the vortex except by mixing across the vortex edge.

[16] The vortex edge definition used in the model simulations is closely related to the “kinematic edge” defined by *Pierce and Fairlie* [1993]. The vortex edge is determined by integrating Q and vorticity around rotational streamlines of the flow. The northernmost streamline with negative integrated Q and positive (cyclonic) integrated vorticity defines the edge of polar vortex. This kinematic edge typically resides on the polarward flank of the polar night jet [*Pierce et al.*, 1994], is similar to dynamical vortex edge definitions such as defined by *Nash et al.* [1996] but is associated with a minimum in the stretching rates of material lines (minimum Liapunov exponent) instead of sharp gradients in potential vorticity. To assure that the physical characteristics of the kinematic boundary are accurately represented in the model we do not allow enhanced mixing to occur across the edge of the vortex. Consequently, the diffusion during a particular model time step does not significantly affect the mean mixing ratios within the vortex. However, as trajectories descend within the Arctic vortex they mix with different populations at different altitudes. Consequently, the coupling between diabatic descent and mixing can change the mean mixing ratio within the vortex at a given altitude.

### 3. The Solve LaRC LCTM Simulation

[17] The model was integrated from 1 October 1999 to 28 March 2000. Trajectories from 1995 HALOE and 1312 POAM III occultations were included in the model integra-

tion. Individual trajectories were allowed to exist for 60 days. This long lifetime of the trajectories introduces errors in the trajectory position (particularly longitude) but by considering the ensemble mean of a large number of trajectories the effects of these errors are minimized [*Pierce et al.*, 1999]. Figure 1 shows the sampling characteristics of the HALOE and POAM III occultation measurements over the course of the 1999/2000 winter along with zonal mean wind speeds at 450K. In the October–November time period (Julian days –90 through –30) HALOE sampled extensively equatorward of 60°N with measurements within the vortex during the northern most extent of the orbit. POAM III measurements became available at the beginning of November (Julian day –60) and sampled poleward of 60°N. HALOE experienced data losses due to elevated instrument temperatures and limited spacecraft power during much of November 1999. The Arctic vortex was just beginning to form at this time with wind speeds generally near 15 m/s at 450K. During the December–January time period (Julian days –30 through 30) POAM III sampled generally poleward or near the core of the mean polar night jet at 450K while HALOE provided primarily midlatitude measurements to the south of the jet, which strengthened during this period, reaching mean wind speeds up to 32 m/s in January. HALOE experienced additional data losses during late January and early February. During the February–March time period (Julian days 30 through 90) the Arctic vortex showed more transient behavior with a rapid deceleration of the zonal mean 450K jet during the last half of February. POAM III and HALOE sampled both inside and outside the Arctic vortex during this time period.

[18] During the SOLVE deployments we found that the ensemble trajectories initialized from the HALOE and POAM III measurements did not adequately sample the cold pool within the interior of the Arctic vortex in the lower stratosphere (ensemble averaged trajectory temperatures were considerably warmer than the mean vortex temperatures obtained from the UKMO assimilation). To alleviate this sampling bias we developed a cold pool initialization procedure, which involves “spawning” of new “daughter” trajectories near the “parent” trajectory. Each daughter has the same chemical characteristics as the parent and was initialized 100 m in front of its parent along the trajectory path. Shear deformation leads to the dispersal of the daughter trajectories with time. Conditions for spawning were evaluated once every 2 days (at 12Z) throughout the integration and spawning occurred whenever the parent trajectory age was greater than 30 days, the latitude was greater than 30°N, and the temperature was less than 192.5K. As will be shown, the cold pool initialization resulted in improved sampling of the cool pool. The spawning procedure means that a particular parent trajectory can potentially spawn a number of different daughter trajectories, particularly if it remains within the cold pool for a number of days, effectively extending its lifetime. However, no new chemical information is being added to the simulation and the cold pool initialization merely improves the sampling characteristics of the ensemble trajectory simulation.

[19] The first 60 days of the simulation (October–November 1999) are considered a “spin-up” period during which the Arctic vortex forms and the HALOE and

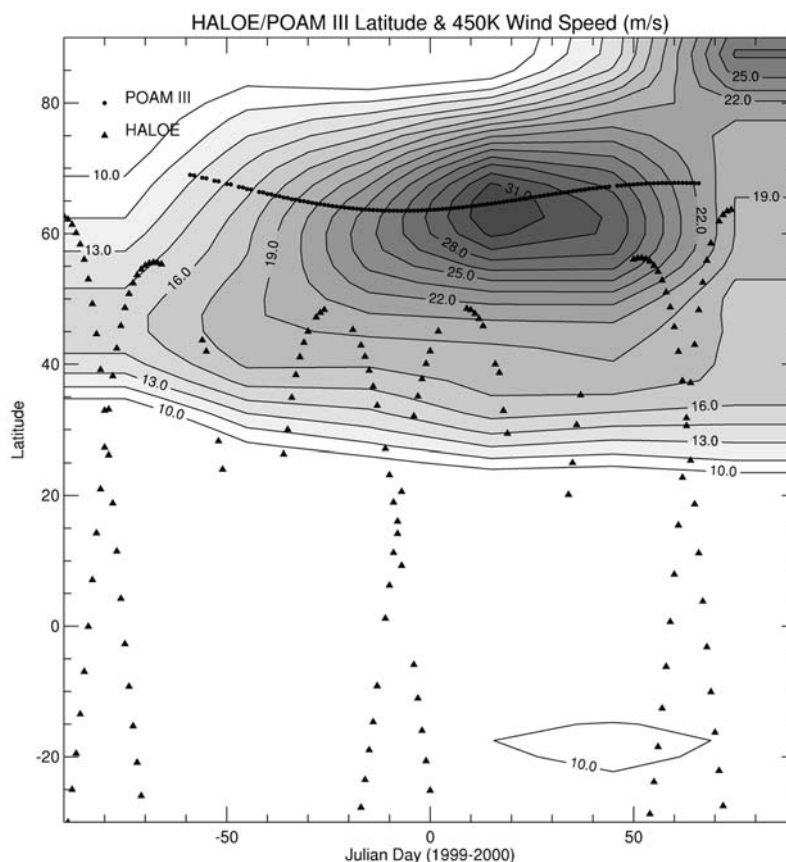


**Figure 1.** Sampling characteristics of the HALOE and POAM occultation measurements between October 1999 (Julian day  $-90$ ) and March 2000 (Julian day  $90$ ). Circles are POAM III occultation points and triangles are HALOE occultation points. The zonal mean wind speed (m/s) on the 450K potential temperature surface is contoured.

POAM III trajectories accumulate. The rest of this paper will focus on the December–March 1999/2000 portion of the simulation.

### 3.1. Comparisons With Early Winter Balloon FTIR Measurements

[20] On 3 December 1999 the balloonborne MkIV Fourier transform infrared (FTIR) solar absorption spectrometer [Toon, 1991] was launched into the core of the Arctic vortex (equivalent latitude of  $80^{\circ}\text{N}$ ). The intent of this flight was to characterize the state of the Arctic vortex in early winter. Comparisons between the single MkIV profile and the range of mixing ratios predicted by the LaRC LCTM provides an assessment of how well the MkIV profile represents the vortex as a whole. The MkIV measurements also provide an opportunity to assess the LaRC LCTM predictions during the early winter, and establish how well the model has characterized the Arctic vortex prior to the period of enhanced photochemical loss. Figure 2 shows observed profiles of  $\text{O}_3$ ,  $\text{NO}_y$ , and  $\text{Cl}_y$  as a function of potential temperature, along with the individual trajectory predictions of these species concentrations within the vortex, and the predicted vortex ensemble mean profiles. A synoptic map of the distribution of the ensemble ozone prediction at 575K–625K is also shown. The bold black line in the synoptic map shows the edge of the Arctic vortex at 600K, the thick, short

black line over Sweden is the trajectory of the MkIV, and the contours indicate the wind speed at 600K.

[21] The observed  $\text{O}_3$  profile falls within the range of ensemble ozone mixing ratios predicted by the model but is clearly on the lower side of the model prediction, which shows a wide range of  $\text{O}_3$  mixing ratios within the vortex above approximately 500K. Trajectories initialized with HALOE and POAM III observations show a similar spread in  $\text{O}_3$  mixing ratios although those initialized with HALOE data tend to show a bimodal distribution above 800K while those initialized with POAM III observations are more uniformly distributed between high and low mixing ratios. The origin of the bimodal HALOE  $\text{O}_3$  is not immediately clear. Investigation of the initial characteristics of these trajectories establishes that it is not associated with the latitude, time, or altitude at which the HALOE measurement occurred. However, the synoptically mapped ensemble  $\text{O}_3$  distribution shows that the low  $\text{O}_3$  mixing ratios are found in the interior of the Arctic vortex, well poleward of the polar night jet, while the higher  $\text{O}_3$  mixing ratios are found near the edge of the vortex at these potential temperatures.

[22] The predicted vortex ensemble mean  $\text{NO}_y$  and  $\text{Cl}_y$  profiles are very close the observed MkIV profiles between 400K and 900K with mean absolute differences of 11% and 6%, respectively indicating that mixing ratios for the chlorine and nitrogen reservoirs are well characterized by

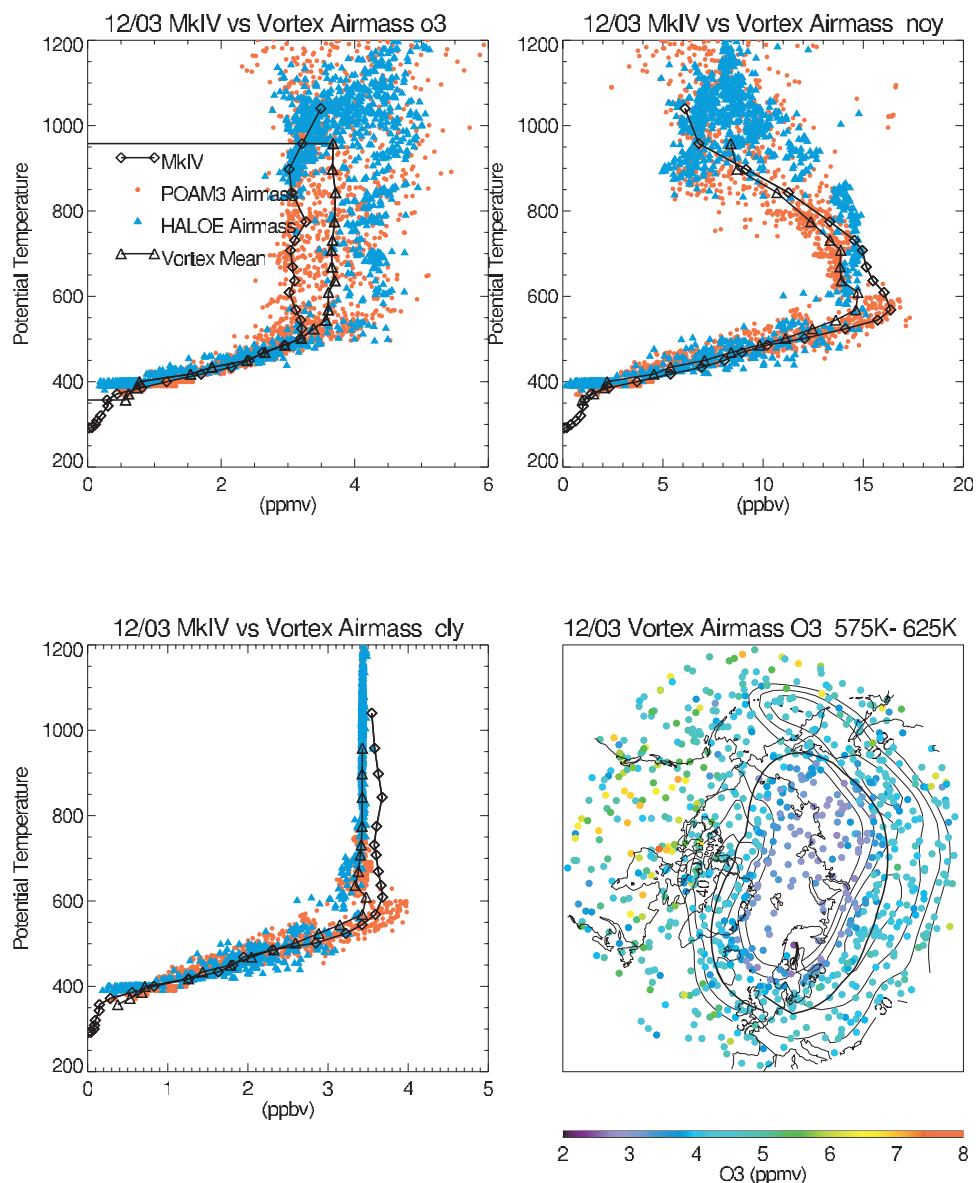


**Figure 2.** Vertical profiles of O<sub>3</sub>, NO<sub>y</sub>, and Cl<sub>y</sub> observed by the MkIV FTIR instrument and predicted by the model on 3 December 1999 (12/03). The observed profile is indicated by the line with diamonds. The predicted vortex ensemble mean profile is indicated by the line with triangles. Individual vortex trajectory mixing ratios are indicated by red circles for trajectories initialized from POAM III occultations and blue triangles for trajectories initialized from HALOE occultations. A synoptic map of the distribution of the ensemble ozone prediction (ppmv) at 575K–625K is shown in the lower right panel. The bold black line in the synoptic map shows the edge of the Arctic vortex at 600K, the thick, short black line over Sweden is the trajectory of the MkIV. The contours indicate the wind speed (m/s) at 600K.

the PV and CH<sub>4</sub> mapped IMPACT model climatology at these altitudes. The comparison between the LaRC LCTM ensemble NO<sub>y</sub> and Cl<sub>y</sub> predictions and MkIV observations indicate that the observed profile provides a reasonable characterization of the mean characteristics of the early 1999/2000 winter vortex below 800K.

[23] The LaRC LCTM predictions indicate that there was a radial gradient in the O<sub>3</sub> mixing ratios within the Arctic vortex at 600K. A similar distribution of O<sub>3</sub> within the early winter Arctic vortex was found by Kawa et al. (unpublished manuscript, 2001). However, our vortex edge definition

suggests that the O<sub>3</sub> gradient begins within the vortex while Kawa et al. found that the gradient lies between the inner and outer vortex edge defined by Nash et al. [1996]. This apparent discrepancy arises due to particularly large differences between the Nash vortex edge and the kinematic edge on this day. On average, the differences between the kinematic edge and the Nash et al. [1996] edge are negligible. Comparisons between the Nash et al. [1996] and kinematic edge during the SOLVE time period (not shown) indicate that mean differences are less than 2° in equivalent latitude, with the kinematic edge systematically equatorward of the

Nash edge. Consequently, the kinematic edge is roughly equivalent to the “outer” edge as defined by *Nash et al.* [1996]. What is clear from Figure 2 is that the radial gradient in  $O_3$  at 600K is poleward of the polar night jet core. As will be shown later, air from 500K to 600K is advected poleward and then descends to near 450K by spring where it experiences enhanced photochemical loss. Because of this descent, the  $O_3$  mixing ratios between 500K and 600K during early winter play a critical role in observational determinations of the photochemical loss rates. The range of  $O_3$  mixing ratios predicted within the vortex at 600K during the beginning of December complicates the diagnosis of springtime photochemical ozone loss in the lower stratosphere from observed  $O_3$ -tracer correlations. The LaRC LCTM predictions, which are initialized with observed  $O_3$ , suggest that assuming that a few early winter  $O_3$  profiles can characterize the “initial” state of the Arctic vortex may be an unrealistic assumption.

[24] A number of different photochemical, microphysical, and diffusive processes must be simulated along each trajectory to accurately represent the mean vortex evolution. Figure 3 illustrates these processes for a typical vortex trajectory. This particular trajectory was spawned from a trajectory originating from a POAM III observation at 525K. The trajectory was initialized in the beginning of December 1999 at 517K and descended to 406K during its lifetime. It remained within the vortex until late March, making numerous orbits around the Arctic vortex and encountering temperatures below 195K for extended periods of time between late December and mid-January (Julian days -10 to 20). Two periods were cold enough for ice formation. The trajectory spent most of December and January orbiting in and out of the region of continuous polar night with typical daylight exposure times of 6 hrs per day (0.25 daylight fraction). By late January (Julian day 30) the daylight exposure of the trajectory began to increase while the  $O_3$  mixing ratio of the trajectory begins to show more rapid declines. Diffusive  $O_3$  tendencies can be quite large but very episodic as the trajectory moves in and out of regions of enhanced mixing within the vortex. Diffusive tendencies account for much of the high frequency variation in the  $O_3$  mixing ratio along the trajectory. Enhanced photochemical ozone loss occurs during periods of higher daylight fraction. During December through mid-January, the peak net loss rates (production-loss:  $O_3$  P-L in Figure 3) for this particular trajectory range from 20 to 40 ppbv/day. By late January the net loss rates accelerate with peak loss rates near 70 ppbv/day occurring at the beginning of March (Julian day 60). Chlorine activation, diagnosed from the  $Cl_x/Cl_y$  ratio, begins in early December and reaches nearly 80% by mid-January. This particular trajectory shows chlorine deactivation from late January through February and then a period of reactivation in March associated with colder temperatures near Julian day 60.

[25] The trajectory  $NO_y$  shows a series of small declines during December, prior to the first encounter with temperatures below ice frost points. These declines are associated with the formation of condensed-phase  $HNO_3$  and subsequent sedimentation, which removes  $HNO_3$  from the trajectory  $NO_y$  at about 0.3 ppbv/day. The first ice event for this trajectory occurs during the last week of December (Julian day -5) with declines in  $NO_y$  of approximately 3

ppbv/day, associated with sedimentation of  $HNO_3$ . This ice event occurs during a period of high diffusive tendencies that offset much of the denitrification tendencies. The largest change in  $NO_y$  is associated with a strong diffusive mixing event in the beginning of January that results in significant reductions in the trajectory  $NO_y$ . This mixing event is followed by a second ice event that occurs in early January (Julian day 10) and brings the  $NO_y$  mixing ratio of the trajectory to nearly zero. This complex interaction between sedimentation and mixing occurs as diabatic descent and localized sedimentation leads to the development of sharp  $NO_y$  gradients within the vortex and neighboring trajectories with a wide range of  $NO_y$  mixing ratios mix.

[26] It is clear from the evolution of this single vortex trajectory that each trajectory encounters a broad range of chemical and dynamical environments over the course of the winter. To accurately characterize the evolution of the Arctic vortex one must look at the statistics of a number of trajectories to determine the ensemble mean state of the vortex. Ensemble averaging is accomplished by daily binning all vortex trajectories in potential temperature bins defined by the isentropic database and averaging to determine daily profiles of the vortex ensemble mean chemical and dynamical characteristics. Time series of the vortex ensemble mean evolution are presented in the next section.

### 3.2. Vortex Ensemble Mean Evolution

[27] Figure 4 shows the time series of the vortex averaged temperatures obtained from the gridded UKMO temperatures, as well as ensemble averages of initial potential temperature, condensed  $HNO_3$  (NAT), and temperature for all vortex trajectories as a function of potential temperature. The Arctic cold pool forms above 500K during the later half of December 1999. The cold pool gradually descends over the course of the winter with vortex averaged UKMO temperatures remaining below 202K until the end of January 2000. *Manney et al.* [2002] compared 1999/2000 Arctic temperatures from a number of different assimilation centers including UKMO. They found that the UKMO cold pool was significantly larger than found other assimilation data sets during January 2000, and that the UKMO coldest temperatures were generally colder than other assimilated temperatures. However, trajectory studies conducted by *Manney et al.* [2002] indicated that the UKMO temperature cold bias did not result in significant bias in the extent of PSC exposure. During the beginning of February there is a minor disturbance that results in a temporary warming of the vortex, but colder temperatures return by mid-February and persist until mid-March, when the final warming begins and the vortex temperatures warm rapidly. Diabatic descent is evident in the ensemble mean initial potential temperature of the vortex trajectories. Trajectories that originated at 550K are found at 475K during early December and descend to 450K by late February and early March. The 550K isentrope is near the lower limit of altitudes within the vortex with a wide range of  $O_3$  mixing ratios in early December (see Figure 2). The overturning of the initial isentropes during mid-February is a consequence of intrusions of middle latitude air into the vortex at 500K. The ensemble mean

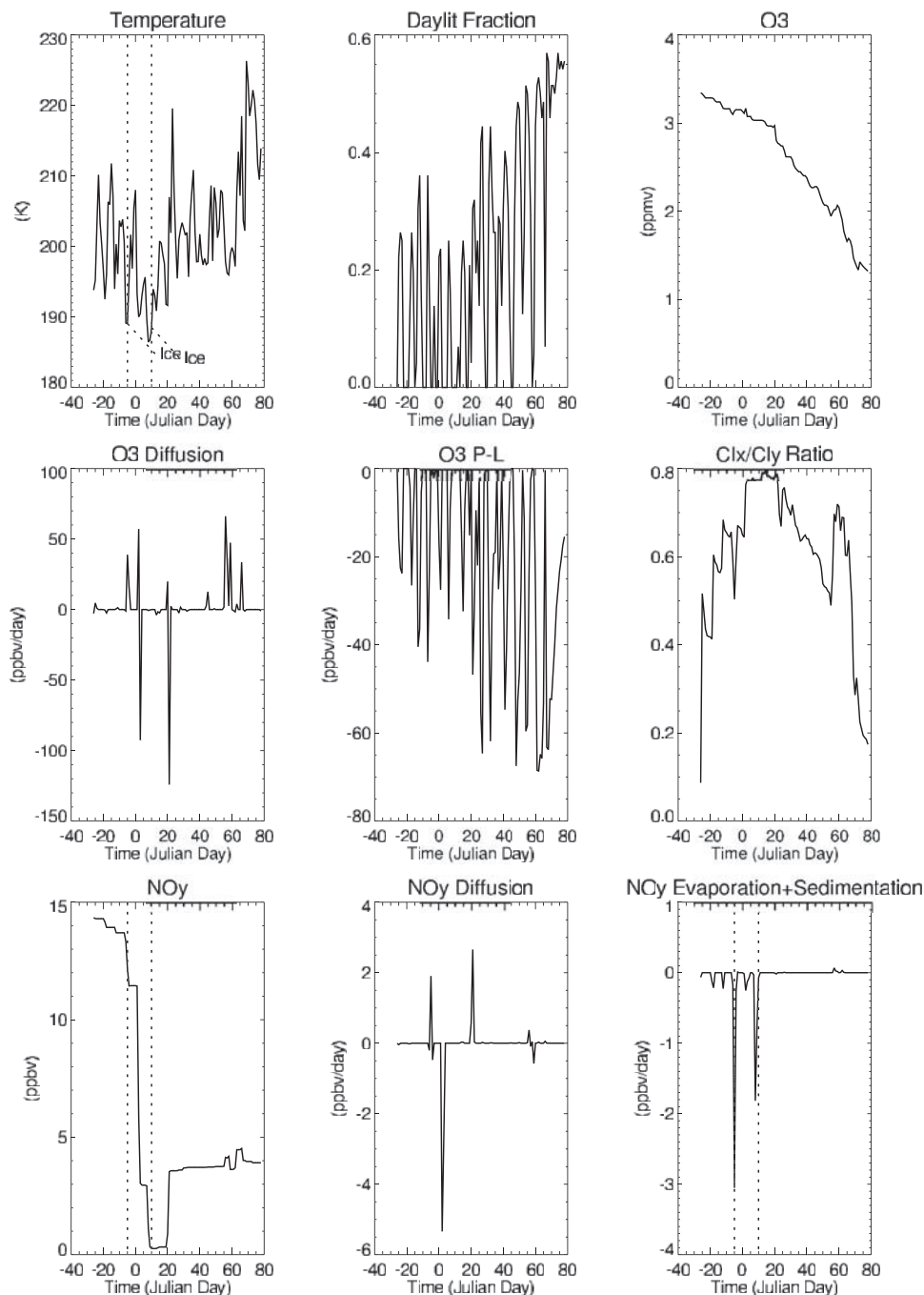


**Figure 3.** Time series of photochemical, microphysical, and diffusive processes along a typical vortex trajectory. Panels in the upper row show trajectory temperature (K), daylight fraction, and O<sub>3</sub> mixing ratio (ppmv). Panels in the middle row show diffusive and photochemical tendencies (ppbv/day), and the ratio of Cl<sub>x</sub>/Cl<sub>y</sub> for the trajectory. Panels in the bottom row show the trajectory NO<sub>y</sub> mixing ratio (ppbv), and diffusive and evaporation + sedimentation tendencies (ppbv/day). The vertical dotted lines indicate days which ice PSCs were encountered by the trajectory. Time is indicated by Julian day beginning 20 November (Julian day -40).

condensed-phase HNO<sub>3</sub> indicates the presence of PSCs within the vortex. PSCs initially form at the beginning of December between 500K and 550K and grow in-depth to between 400K and 600K (15.5 and 23.5 km) by late December. The PSCs persist within the vortex until early February, when warming of the vortex results in evaporation

of the NAT particles. Limited PSCs reappear during late February and early March between 400K and 450K.

[28] The ensemble mean temperatures from the LaRC LCTM trajectories capture the vertical and temporal variability found in the vortex averaged UKMO gridded temperatures very well. This agreement between the evolution of the

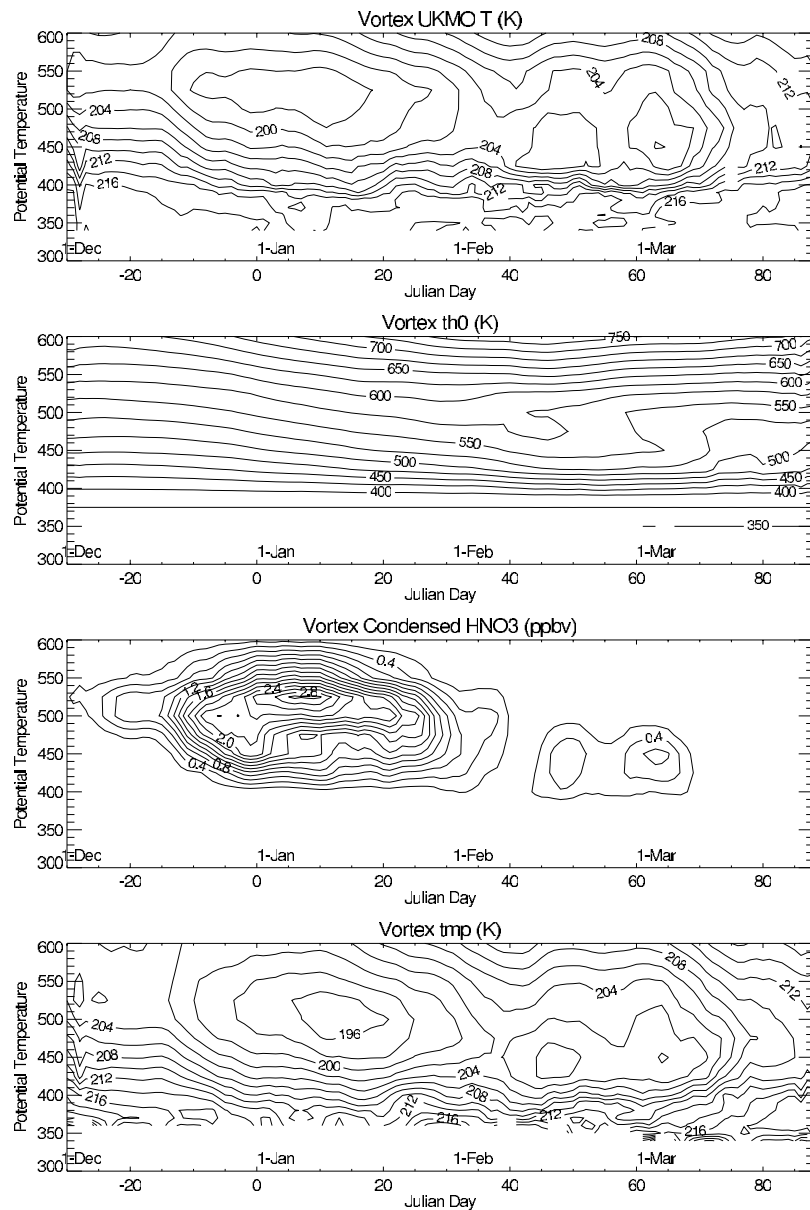


**Figure 4.** Potential temperature-time series of the vortex averaged temperatures (K) obtained from the gridded UKMO temperatures (upper panel) and vortex ensemble means of initial potential temperature ( $Th_0$ ), condensed  $HNO_3$  (NAT) (ppbv), and temperature (tmp) (K). The first day of each month is indicated.

ensemble mean temperatures and the evolution of the vortex averaged UKMO gridded temperatures indicates that the LaRC LCTM is adequately sampling the meteorological conditions within the Arctic vortex during this period. However, the coldest ensemble mean vortex temperatures are 2K colder than the coldest vortex averaged UKMO temperatures during mid-January and late February. The colder ensemble mean temperatures during this period arise because of the dense sampling within the Arctic cold pool associated with the cold pool initialization procedure discussed previously. This sampling, coupled with the general cold bias in the UKMO temperatures (S. Buss et al., Arctic stratospheric temperature in the winters 1999/2000 and 2000/2001: A quantitative assessment and microphysical implications,

submitted to *Journal of Geophysical Research*, 2001) will tend to bias the LaRC LCTM results toward a more extensively processed vortex than may have actually occurred.

[29] Figure 5 shows time series of ensemble mean vortex  $NO_y$  and  $NO_x$  tendencies due to evaporation-sedimentation, diffusion, and vertical advection. The ensemble mean absolute amplitude of the diffusive tendencies is shown to identify time periods where diffusive tendencies are likely to play a significant role in determining the constituent distributions within the vortex. (Recall that diffusive tendencies have negligible effect on the vortex ensemble mean). The ensemble mean vertical advection tendency is obtained by determining the ensemble mean diabatic descent rate and multiplying it by the vertical gradient of

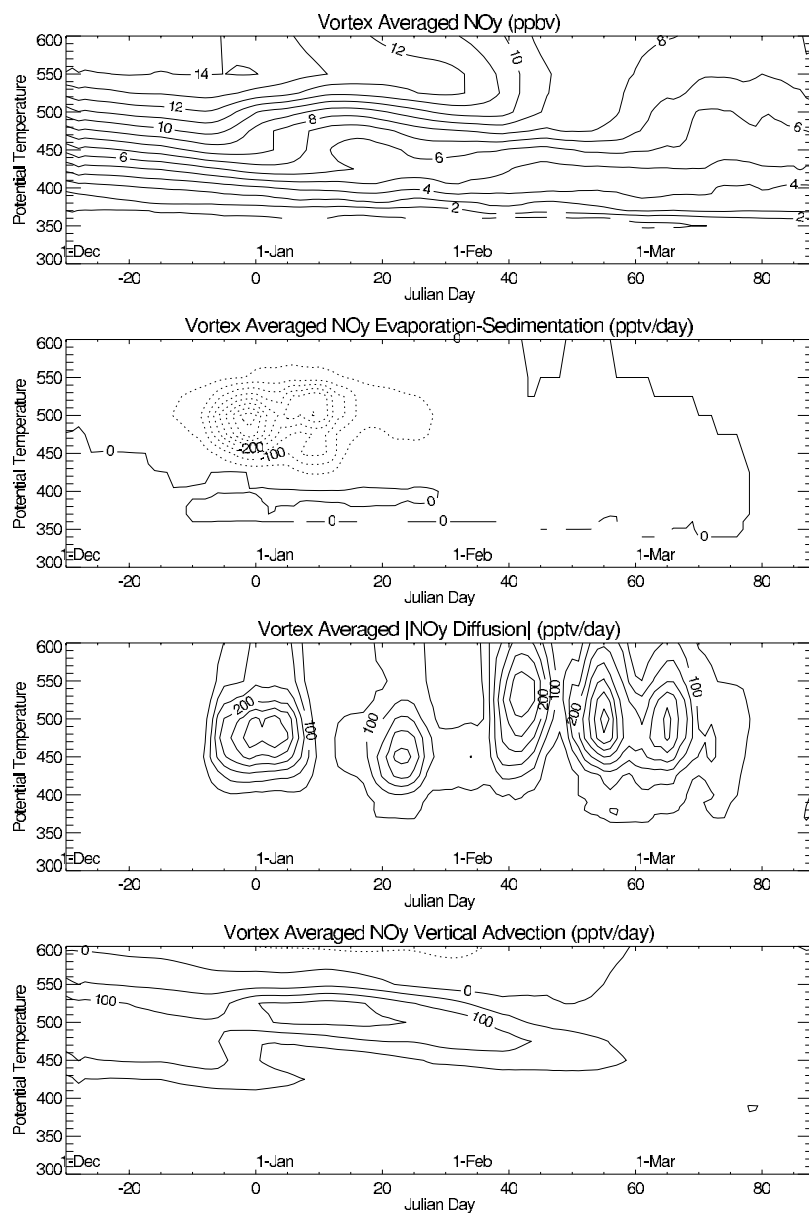


**Figure 5.** Potential temperature-time series of vortex ensemble mean NO<sub>y</sub> (ppbv), NO<sub>y</sub> evaporation plus sedimentation tendency (pptv/day), absolute value of NO<sub>y</sub> diffusive tendency (pptv/day), and NO<sub>y</sub> vertical advection tendency (pptv/day). Negative tendencies are indicated by dashed contours. The first day of each month is indicated.

the ensemble mean vortex NO<sub>y</sub> using potential temperature as a vertical coordinate.

[30] NO<sub>y</sub> isopleths gradually descend due to vertical advection during the first half of December 1999 with negligible contributions from evaporation, sedimentation, or diffusion. By late December the extent of cold temperatures becomes large enough for significant sedimentation of condensed HNO<sub>3</sub> to occur and the vortex is denitrified at a rate of over 400 pptv/day. This rapid denitrification occurs in conjunction with dehydration that reduces the ensemble mean H<sub>2</sub>O by 30 ppbv/day during the same period (not shown). Comparison with Figure 4 (THO and condensed HNO<sub>3</sub>) shows that this period of intense sedimentation corresponds to a period where the isopleths of condensed HNO<sub>3</sub> descend more rapidly than the initial potential

temperature isopleths between 500K and 450K, indicating cross-isentropic exchange of condensed-phase HNO<sub>3</sub> via evaporation of falling particles. Vertical advection of higher NO<sub>y</sub> continuously resupplies NO<sub>y</sub> at a rate of 150 pptv/day near the top of the cold pool. Local NO<sub>y</sub> losses due to denitrification overwhelm the ability of vertical advection to resupply NO<sub>y</sub> within the cold pool as is clearly evident in the rapid decline in ensemble averaged NO<sub>y</sub> during January. This period of rapid denitrification terminates by mid-January leaving approximately 5–6 ppbv of NO<sub>y</sub> at 450K throughout the rest of the winter. Vertical advection continues to bring down higher NO<sub>y</sub> from aloft at altitudes between 450K and 550K while vertical advection reduces NO<sub>y</sub> mixing ratios above 550K. The ensemble mean absolute amplitude of the NO<sub>y</sub> diffusive tendency shows strong

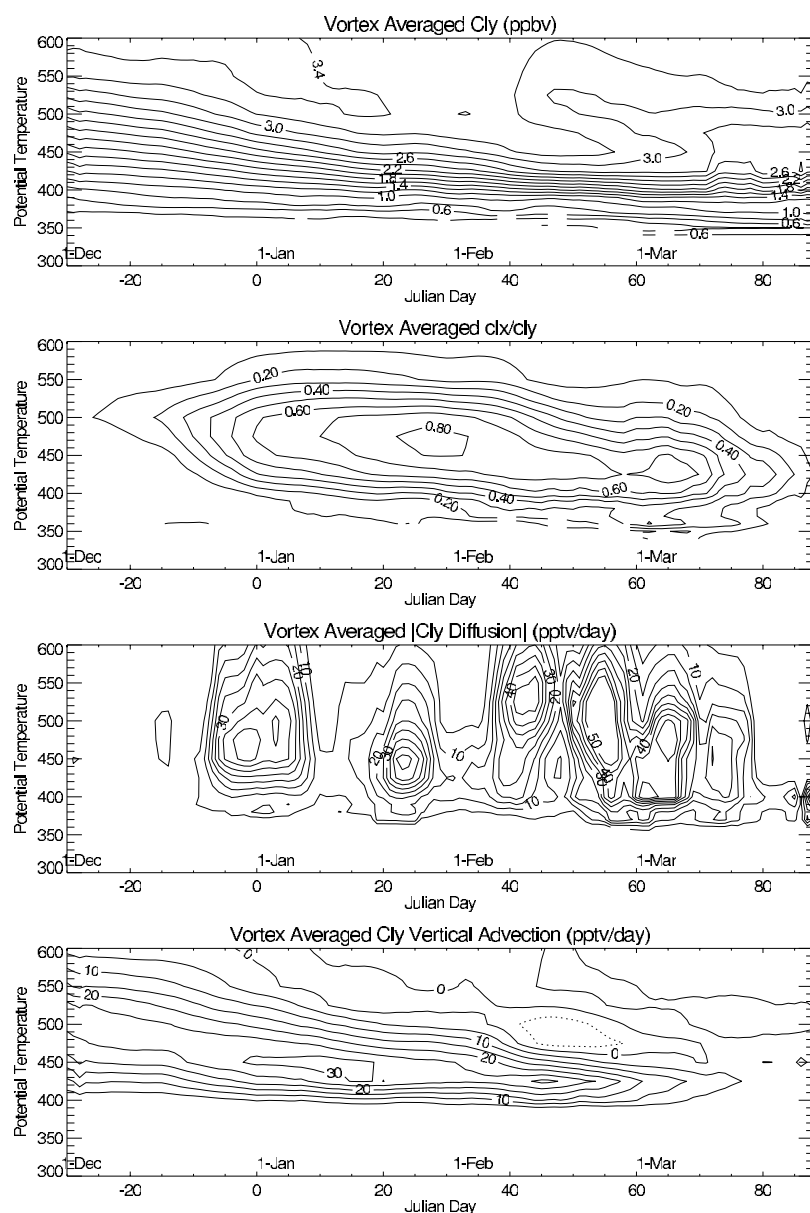


**Figure 6.** Potential temperature-time series of vortex ensemble mean  $Cl_y$  (ppbv),  $Cl_x/Cl_y$  ratio, absolute value of  $Cl_y$  diffusive tendency (pptv/day), and  $Cl_y$  vertical advection tendency (pptv/day). Negative tendencies are indicated by dashed contours. The first day of each month is indicated.

mixing within the vortex during the period of rapid denitrification, as local denitrification and vertical advection leads to large horizontal gradients in  $NO_y$ , and then a series of diffusive mixing events in February and early March. There are episodic periods where the ensemble mean absolute amplitude of the diffusive tendencies are comparable with the tendencies due to sedimentation.

[31] Figure 6 shows time series of ensemble mean vortex  $Cl_y$ ,  $Cl_x/Cl_y$ , absolute amplitude of diffusive tendencies, and vertical advection tendencies. Throughout most of the winter the  $Cl_y$  isopleths descend due to vertical advection.  $Cl_y$  has no significant loss processes in the lower stratosphere but the partitioning of the chlorine species within  $Cl_y$  plays a critical role in the enhanced ozone loss in the Arctic spring [Solomon, 1999]. Chlorine reservoir species (HCl

and  $ClNO_3$ ) are converted into chlorine radicals ( $Cl_x = ClO + 2 \cdot Cl_2O_2$ ) during late December 1999 and throughout January 2000, leading to ensemble mean  $Cl_x/Cl_y$  ratios in excess of 0.8 between 450K and 500K in late January. Episodes of significant diffusive mixing of  $Cl_y$  within the vortex occur at the same time as the enhanced  $NO_y$  mixing. Vertical advection increases  $Cl_y$  mixing ratios by 30 pptv/day between 500 and 450K leading to a very sharp vertical gradient in  $Cl_y$  near 425K by February. During the second half of February negative  $Cl_y$  tendencies due to vertical advection dominate above approximately 450K, leading to reductions in the ensemble mean vortex  $Cl_y$  mixing ratios.

[32] Figure 7 shows time series of ensemble mean vortex  $O_3$ ,  $O_3$  net photochemical loss (P-L), absolute amplitudes of diffusive tendencies, and vertical advection tendencies.

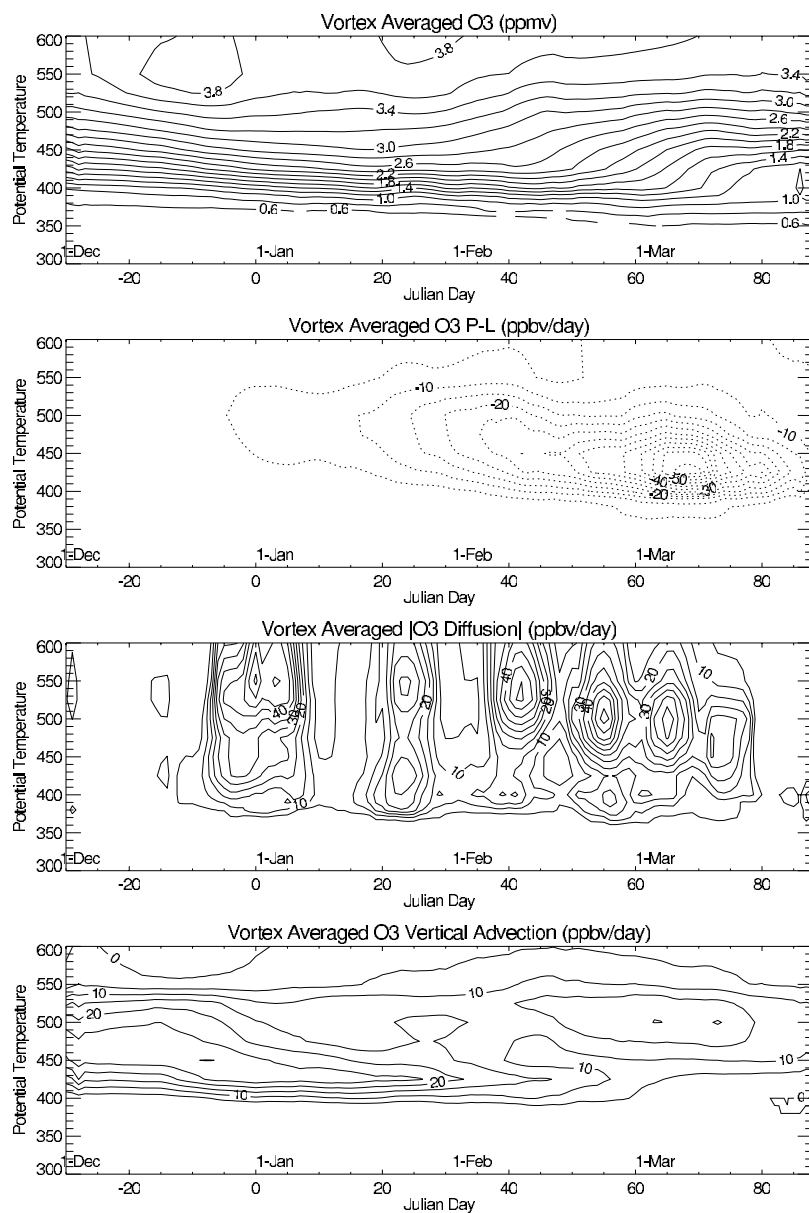


**Figure 7.** Potential temperature-time series of vortex ensemble mean  $O_3$  (ppmv),  $O_3$  photochemical production - loss (P-L) (ppbv/day), absolute value of  $O_3$  diffusive tendency (ppbv/day), and  $O_3$  vertical advection tendency (ppbv/day). Negative tendencies are indicated by dashed contours. The first day of each month is indicated.

Vertical advection, with tendencies that reach 30 ppbv/day at 450K, largely determines the evolution of  $O_3$  in the lower stratospheric Arctic vortex during December to mid-January with only minor contributions from photochemical losses, which are near 5 ppbv/day during early January. There is a period of enhanced photochemical loss between 450K and 500K in mid-February but the major loss occurs at 425K during mid-March, where ensemble mean photochemical loss rates reach over 60 ppbv/day. These rates are very close to the peak loss rates of  $61.6 \pm 4.8$  ppbv/day calculated in mid-March during the 1999/2000 MATCH campaign [Rex *et al.*, 2002]. The ensemble mean absolute amplitude of the  $O_3$  diffusive tendencies shows the same general pattern of episodes of strong diffusion above 450K during February and March as found in  $NO_y$  and  $Cl_y$ . This similarity arises

due to positive vertical gradients in all three constituents below approximately 800K. The link between vertical constituent gradients and diffusive mixing tendencies will be discussed in more detail later.

[33] Figure 8 shows time series of ensemble mean accumulated photochemical  $O_3$  loss and the relative contributions from the  $ClO_x$ ,  $BrO_x$ , and  $ClO_x + BrO_x$  loss cycles to the total photochemical loss. The  $ClO_x$  and  $BrO_x$  loss cycles are defined as given by Wennberg *et al.* [1994]. The accumulated ensemble mean  $O_3$  loss by the end of March is 2.2 ppmv at 450K. This accumulated  $O_3$  loss is slightly less than the peak accumulated  $O_3$  loss of  $2.7 \pm 0.24$  ppmv at 453K obtained by the MATCH campaign [Rex *et al.*, 2002]. Focusing on the periods of significant net loss reveals that  $ClO_x$  and  $BrO_x$  loss cycles each contribute  $\sim 35\%$  to the net

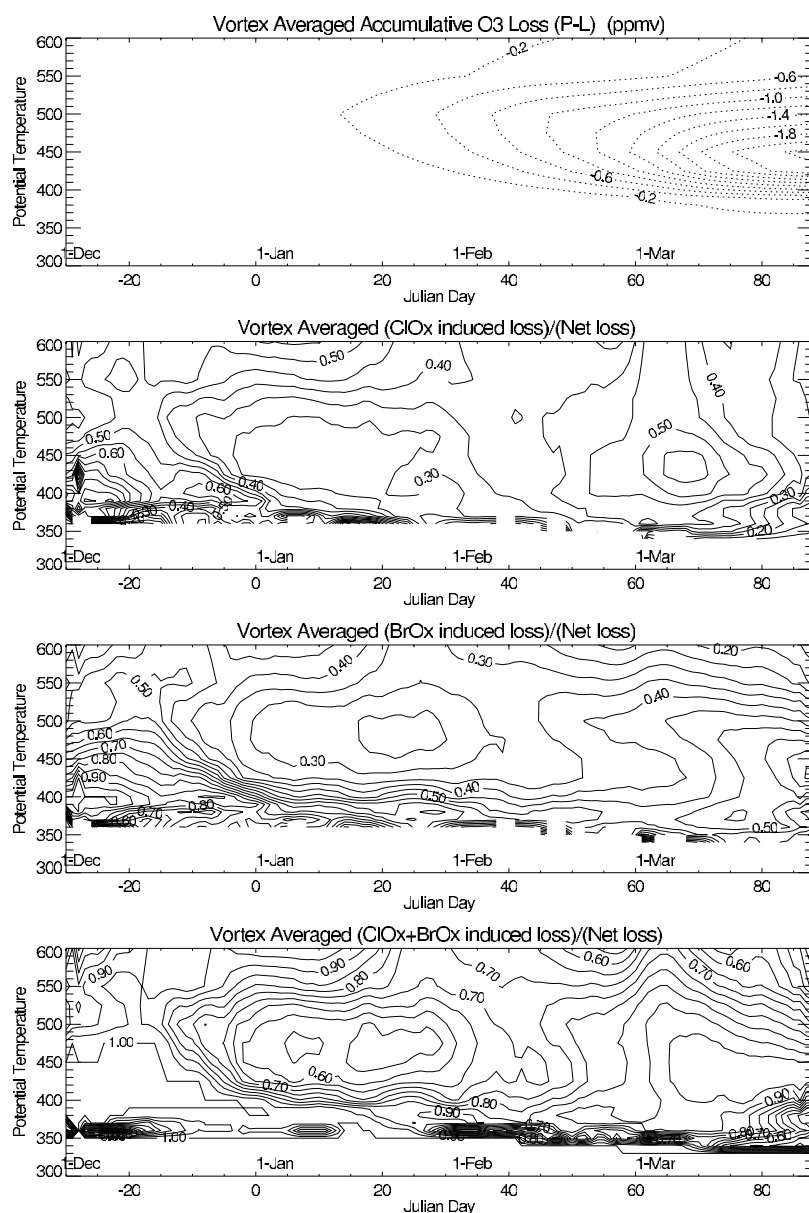


**Figure 8.** Potential temperature-time series of vortex ensemble mean accumulative O<sub>3</sub> photochemical production - loss (P-L) (ppmv), fraction of loss due to ClO<sub>x</sub> cycle, fraction of loss due to BrO<sub>x</sub> cycle, and fraction of loss due to ClO<sub>x</sub> + BrO<sub>x</sub> cycles. Net loss is indicated by dashed contours. The first day of each month is indicated.

loss rates, accounting for 70% of the net loss rates during mid-February. The role of ClO<sub>x</sub> and BrO<sub>x</sub> loss cycles increases to 90–95% of the net loss by March with ClO<sub>x</sub> cycles accounting for 55% and BrO<sub>x</sub> cycles accounting for 40–45%. As the net loss rates decline in mid to late March the relative importance of BrO<sub>x</sub> loss cycles increases while the importance of ClO<sub>x</sub> loss cycles declines. This shift occurs as chlorine recovery takes place and ClO mixing ratios decline. The vortex ensemble mean NO<sub>x</sub> is below 0.01 ppbv (not shown) during early March. Which compares well with the mean NO<sub>x</sub> observed by instruments onboard the ER2 within the vortex during this period (0.02 ppbv). Consequently, the vortex was nearly completely denitrified in early March 2000 and the model predicts that chlorine recovery occurs by transport of extravortex air with lower ClO mixing ratios and higher NO<sub>2</sub> mixing ratios into the vortex.

[34] The ensemble mean time series provide a useful measure of the mean characteristics of the Arctic vortex over the course of the 1999/2000 winter. However, they do not indicate the degree of variability found within the vortex. The next section explores the vortex variability during early March (the period of peak photochemical losses) in detail by comparing predicted frequency distributions with in situ observations from the ER2. These comparisons also serve to establish the validity of the ensemble mean predictions.

### 3.3. Vortex Frequency Distributions

[35] Figure 9 shows frequency distributions (FDs) of CH<sub>4</sub>, O<sub>3</sub>, percent denitrification, and Cl<sub>x</sub>/Cl<sub>y</sub>, for vortex measurements and coincident model trajectories between 425K and 475K taken on the 05/03, 07/03, 11/03, and 12/03

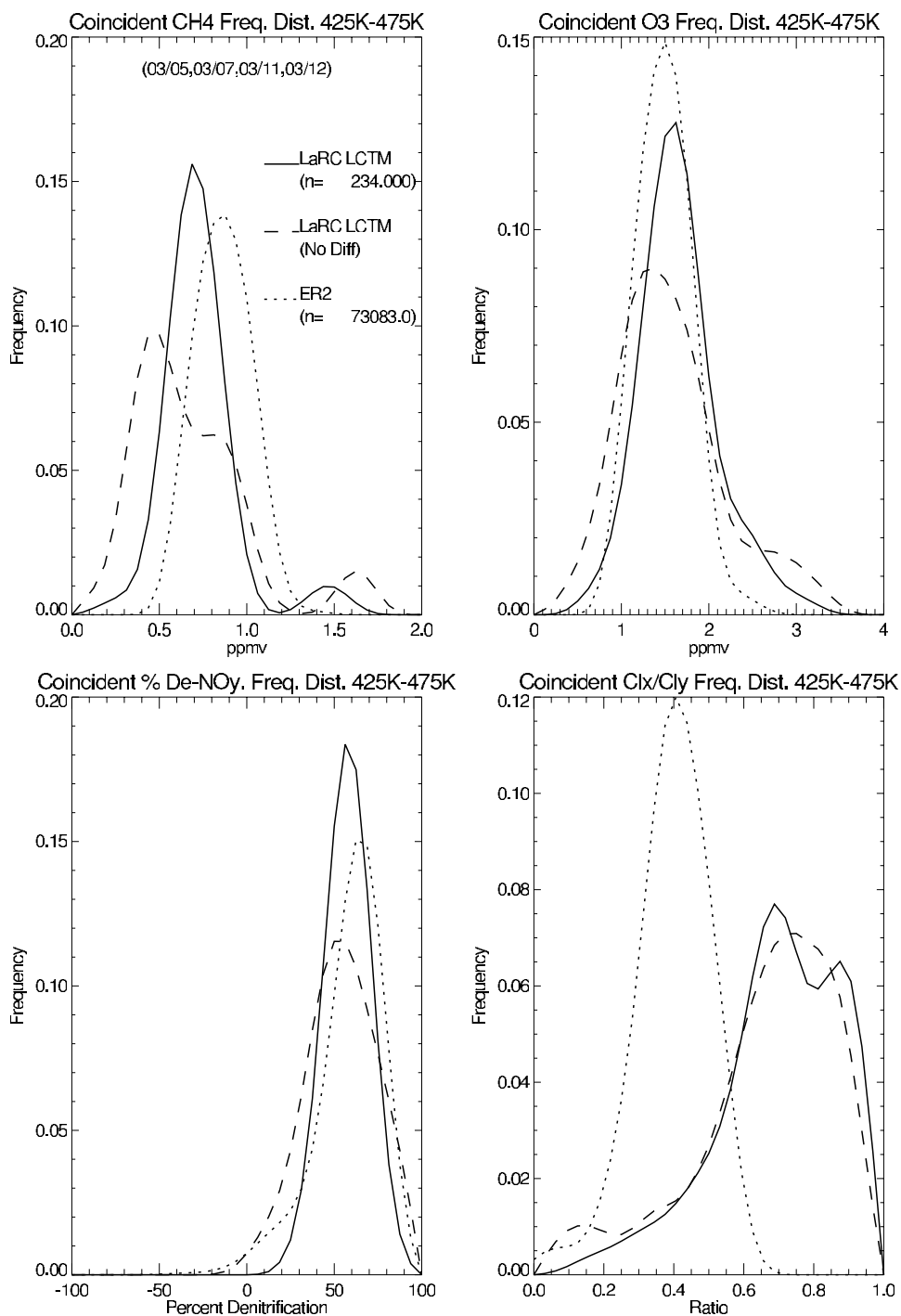


**Figure 9.** Frequency distributions of CH<sub>4</sub>, O<sub>3</sub>, percent denitrification, and Cl<sub>x</sub>/Cl<sub>γ</sub> for vortex in situ measurements (dotted line) and coincident model trajectories between 425K and 475K taken on the 05/03, 07/03, 11/03, and 12/03 ER2 flights. Model frequency distributions are shown for simulations with (solid line) and without (dashed line) diffusive tendencies. The number in parenthesis below the line caption indicates the number of observations/trajectories used to construct the frequency distributions. The coincidence criteria were the same day, 10° longitude, 5° latitude, and 5K in potential temperature.

ER2 flights. The coincidence criteria was the same day, 10° longitude, 5° latitude, and 5K in potential temperature, resulting in 234 coincident trajectories for these flights. Model results include a simulation where diffusive tendencies were turned off to assess the role of diffusion in determining the constituent frequency distributions. The

classification of ER2 measurements as vortex measurements was accomplished by interpolating the vortex marker field in the UKMO isentropic database to the ER2 flight track.

### 3.3.1. CH<sub>4</sub> Frequency Distribution

[36] The CH<sub>4</sub> FD provides the clearest assessment of the impact of diffusion on the simulation since it is long-lived in

the lower stratosphere and its vortex FD is largely determined by the interaction between vertical descent and small-scale diffusion. The predicted vortex CH<sub>4</sub> FD shows a strong peak near 0.7 ppmv. Which is in closer agreement with the observed [Webster *et al.*, 1994] CH<sub>4</sub> FD (peak near 0.9 ppmv) than the simulation without diffusive mixing which peaks near 0.4 ppmv and has a broad shoulder extending to 1.0 ppmv. The differences in the simulations with and without diffusion arise due to differential diabatic descent (which introduces different CH<sub>4</sub> mixing ratios at a given altitude due to the vertical gradient in CH<sub>4</sub>), combined with diffusive mixing which tends to increase the low CH<sub>4</sub> mixing ratios and decrease the high CH<sub>4</sub> mixing ratios. This leads to more uniform CH<sub>4</sub> mixing ratios (narrow peak in the FD) in the simulation with diffusion. However, the model still shows a bias toward low CH<sub>4</sub> mixing ratios. The 0.7 ppmv CH<sub>4</sub> mixing ratio peak found in the predicted FD is close to the ensemble mean vortex CH<sub>4</sub> mixing ratio (0.72 ppmv) at 570K in early December (not shown), which descends at a rate of 1.5K/day during December through January and 0.95K/day during February reaching 450K by early March. Greenblatt *et al.* [2002] used in situ and remote balloon measurements to assess the observed descent rates of selected CH<sub>4</sub> isopleths during the 1999/2000 winter and found that the observed 0.72 ppmv CH<sub>4</sub> isopleth descended from 550K in early December to 470K in early March at a rates of 1.0K/day during December through January and 0.6K/day during February. The larger descent rates in the model CH<sub>4</sub> isopleth implies stronger diabatic cooling in the vortex than actually occurred. In addition to the bias introduced by stronger diabatic descent there is a sampling bias introduced by the cold pool spawning procedure. The trajectories with the lowest CH<sub>4</sub> mixing ratios (near 0.4 in the no-diffusion FD) encountered the cold pool in late December and early January and consequently spawned daughter trajectories. The spawning leads to increased numbers of low CH<sub>4</sub> trajectories that introduce a bias the model FDs toward lower CH<sub>4</sub> mixing ratios.

[37] The modeled CH<sub>4</sub> FDs have a few CH<sub>4</sub> mixing ratios above 1.5. These high CH<sub>4</sub> mixing ratios suggest that there is a small population of extravortex trajectories. These trajectories must have entered the vortex during one of the periods where the kinematic barrier was weakened by transient disturbances, allowing horizontal transport into the vortex to occur. However, the trajectories with high CH<sub>4</sub> mixing ratios make up a very small fraction of the total vortex ensemble, which indicates that, based on the model simulations, horizontal transport of lower stratospheric, extravortex air into the vortex was relatively weak during the 1999/2000 winter.

### 3.3.2. O<sub>3</sub> Frequency Distribution

[38] The O<sub>3</sub> FDs show that the model slightly overestimates the O<sub>3</sub> mixing ratio (peak near 1.6 ppmv) relative to the in situ measurements [Proffitt and McLaughlin, 1983], which show a peak in the FD near 1.5 ppmv at these altitudes, and has a broader tail at high O<sub>3</sub> mixing ratios than is observed. The simulation without diffusion predicts the peak at 1.3 ppmv and the distribution is clearly too broad, particularly on the high O<sub>3</sub> mixing ratio side of the peak. The tail of high mixing ratios in the predicted O<sub>3</sub> could be due to over-sampling of higher initial mixing ratios by HALOE, which does not sample the deep core of the

Arctic vortex at 550K during the early winter as frequently as POAM III does. This initial high bias in the 550K ensemble prediction is evident in Figure 2, which shows that trajectories initialized with HALOE O<sub>3</sub> mixing ratios tend to cluster near the high O<sub>3</sub> portion of the ensemble prediction between 500K and 800K.

### 3.3.3. Percent Denitrification Frequency Distribution

[39] The observed and predicted percent of denitrification within the vortex is determined by subtracting the March in situ NO<sub>y</sub> measurements [Fahey *et al.*, 1989] and ensemble NO<sub>y</sub> predictions from the NO<sub>y</sub> observed during the 12/03 MkIV balloon flight, using N<sub>2</sub>O mixing ratios to identify similar air masses. The 03/05 in situ NO<sub>y</sub> measurements are filtered to exclude PSC encounters since condensed-phase HNO<sub>3</sub> tends to introduce uncertainties in the gas-phase NO<sub>y</sub> measurement. No PSCs were encountered during the rest of the March flights considered here. The predicted and observed distribution of denitrification shows relatively good agreement when diffusion is included although the predicted FD is somewhat narrower than observed with a peak near 60% while the observed peak is near 70% denitrification. The simulation without diffusion shows a broader distribution than is observed with a peak near 50%. The observed denitrification shows a long tail extending toward (and beyond) zero that is not present in the predicted FD and is too broad in the simulation without diffusion.

[40] The 10% differences between the location of the observed and predicted peaks in the percent denitrification FDs indicates that our sedimentation rates may be slightly lower than actually occur. The tail in the observed FD could arise due to re-evaporation of sedimenting NAT particles, incomplete denitrification, or mixing of denitrified air with unprocessed air from aloft. Our simulations indicate that re-evaporation of sedimenting NAT contributes approximately 2 ppbv of NO<sub>y</sub> at these altitudes (shown later). Signatures of mixing with unprocessed air from aloft are evident in the predicted NO<sub>y</sub>/CH<sub>4</sub> correlations (not shown) but these trajectories tend to be found at slightly higher potential temperatures than the ER2 sampled and only make up a small fraction of the vortex ensemble below 475K during March. Consequently, it is most likely that the observed tail is associated with incomplete denitrification in the air sampled by the ER2. The fact that the no-diffusion simulation overestimates this feature while the simulation with diffusion underestimates it suggests that the model diffusion may be somewhat stronger than actual small-scale mixing processes.

[41] The simple bulk equilibrium parameterization of denitrification used in the model is in lieu of full calculations involving detailed representation of the particle microphysics [Drdla *et al.*, 2002]. The agreement of observed and calculated denitrification indicates that the model parameterization captures some important large-scale features of the distribution of denitrified air in the Arctic vortex. However, observations of NO<sub>y</sub>, HNO<sub>3</sub>, and aerosol particles during SOLVE have revealed the presence of large HNO<sub>3</sub>-containing particles over large areas of the vortex in the lower stratosphere [Fahey *et al.*, 2001; Carslaw *et al.*, 2002; Northway *et al.*, 2002] which are not accounted for in the model. Particles with sizes ranging up to 20 microns in diameter were observed throughout late January to mid-March [Fahey *et al.*, 2001]. The small population of large particles suggests a highly selective, nonequilibrium nucle-

ation process must be responsible for the formation of these particles [Fahey *et al.*, 2001]. Instantaneous flux values indicate that these particles could substantially denitrify the lower stratosphere in a matter of days. In contrast, rapid denitrification in the model occurs via synoptic-scale  $\text{HNO}_3$  removal via equilibrium growth of a NAT ( $\text{HNO}_3 \cdot 3\text{H}_2\text{O}$ ) coating on ice particles.

[42] Davies *et al.* [2002] conducted chemical transport model simulations during the 1999/2000 winter using the SLIMCAT model to explore model sensitivity to differences in denitrification parameterizations. They considered two different formulations, an ice formation scheme very similar to our scheme and a NAT scheme that assumed a bimodal size distribution (0.5 micron and 6.5 micron radii) constrained by the Fahey *et al.* [2001] observations. In the bimodal NAT scheme the small mode affects heterogeneous rate calculations due to large surface area densities while the large mode is responsible for the majority of the denitrification due to larger fall velocities. Davies *et al.* [2002] found that both schemes produced extensive denitrification during the 1999/2000 winter when UKMO temperatures were used although the bimodal NAT scheme produced somewhat better agreement with observed denitrification than the ice scheme. In particular, the ice scheme did not reproduce the observed extensive denitrification when ECMWF temperatures were used.

[43] To better understand the role of ice formation in the denitrification processes one must look at in situ water vapor observations. These suggest that at least some of the observed denitrification could have occurred in association with dehydration. In situ measurements of total hydrogen at the highest altitudes sampled by the ER2 (21km) suggest that widespread dehydration of at least 0.2 ppmv occurred for air masses with  $\text{CH}_4$  mixing ratios of 0.7 ppmv, [Herman *et al.*, 2002], and balloon borne instruments indicate dehydration of near 0.5 ppmv at  $\text{CH}_4$  mixing ratios of 0.7 ppmv, [Schiller *et al.*, 2002]. However, in situ observations indicate that while all of the dehydrated air was denitrified, much of the denitrified air was not dehydrated (R. Herman, personal communication, 2001). The majority of the simulated denitrification occurred in conjunction with dehydration.

### 3.3.4. $\text{Cl}_x/\text{Cl}_y$ Frequency Distribution

[44] The observed FD of  $\text{Cl}_x/\text{Cl}_y$  is obtained by combining  $\text{Cl}_y$  measurements from the ACATS IV instrument [Elkins *et al.*, 1996], with  $\text{ClO} + 2 \cdot \text{Cl}_2\text{O}_2$  measurements from the Harvard  $\text{ClO}_x$  instrument (R. Stimpfle *et al.*, unpublished manuscript, 2001). The observed  $\text{Cl}_x/\text{Cl}_y$  FD peaks near 0.4 while LaRC LCTM simulations with and without diffusion both show  $\text{Cl}_x/\text{Cl}_y$  FDs which peak near 0.7–0.9 with long tails toward low  $\text{Cl}_x/\text{Cl}_y$  ratios. Diffusive mixing doesn't significantly change the partitioning of  $\text{Cl}_x$  within the  $\text{Cl}_y$  family. The high ratio of predicted  $\text{Cl}_x/\text{Cl}_y$  relative to the observed ratio is larger than can be explained by uncertainties in the observed  $\text{Cl}_x$  (approximately 30%), and indicates that the model chlorine is significantly overactivated relative to the measurements during early March.

### 3.3.5. Chlorine Frequency Distributions

[45] To further explore the large differences between the modeled and measured chlorine activation levels we consider the partitioning within the  $\text{Cl}_y$  family. Figure 10 shows FDs of observed and modeled  $\text{Cl}_x$ ,  $\text{Cl}_y$ ,  $\text{ClNO}_3$ , and  $\text{HCl}$ .

The  $\text{Cl}_y$  FDs also show the sum of the observed  $\text{ClNO}_3 + \text{ClO} + 2\text{Cl}_2\text{O}_2 + \text{HCl}$ . The  $\text{Cl}_x$  and  $\text{Cl}_y$  FDs show that much of the bias in the model  $\text{Cl}_x/\text{Cl}_y$  occurs because of high model  $\text{Cl}_x$  since the modeled  $\text{Cl}_y$  is in excellent agreement with the ACATS measurements when diffusion is included. The peak in the sum of the observed chlorine species FD is 1.0 ppbv lower than the observed  $\text{Cl}_y$ . This difference reflects an imbalance in the observed chlorine budget of approximately 33%. The response of the model  $\text{Cl}_y$  FD to diffusive mixing mirrors the  $\text{CH}_4$  FD response since both are conserved in the lower stratosphere and  $\text{Cl}_y$  has a positive vertical gradient while  $\text{CH}_4$  has a negative vertical gradient. The excellent agreement between the modeled and measured  $\text{Cl}_y$  occurs in spite of the bias in the modeled  $\text{CH}_4$  since  $\text{Cl}_y$  is nearly uniform above 500K (Figure 2).

[46] The observed FDs of the chlorine reservoir species ( $\text{ClNO}_3$  and  $\text{HCl}$ ) show peaks near 0.4 and 0.3 ppbv respectively, indicating that some chlorine recovery has begun for the majority of the air masses observed by the ER2 during early March. In contrast, the model  $\text{ClNO}_3$  and  $\text{HCl}$  FDs show peaks near zero, indicating that most of the coincident trajectories are still highly activated. The imbalance in the observed chlorine budget does not allow a clear assessment of the model  $\text{Cl}_x/\text{Cl}_y$  bias since underestimates in any of the observed chlorine species or overestimates in the total inorganic chlorine could account for the observed deficit. Increases the observed  $\text{Cl}_x$  would result in better agreement between the modeled and measured  $\text{Cl}_x/\text{Cl}_y$ , while increases in the observed  $\text{ClNO}_3$  or  $\text{HCl}$  would result in worse agreement. However, the FD comparisons between the modeled and measured chlorine species all indicate that the model chlorine activation is high relative to the measurements.

## 4. Synoptic Case Studies

[47] Results from the ensemble mean time series and FD analysis raise two unanswered questions. The first question is how does small-scale diffusive mixing contribute to changes in distribution of trace gas concentrations within the vortex? The second question is why does the model chlorine remain activated during early March? This second question is particularly critical to address since the success in predicting the observed ozone distribution is largely do to a relatively short period of rapid, chlorine catalyzed ozone losses in early March, just prior to chlorine deactivation, during a period of rapidly changing chlorine partitioning and significant overestimates in modeled  $\text{Cl}_x$  relative to the measurements. To answer these questions and illustrate the degree of spatial variability within the vortex we consider two synoptic case studies.

### 4.1. Case Study: 02/26/00

[48] The first case study considers the synoptic situation during the ER2 flight of 02/26/00. This flight occurred during one of the episodes of large ensemble mean amplitudes in diffusive tendencies (see Figures 5, 6, and 7). Figure 11 shows synoptically mapped ensemble predictions of diabatic heating rates, diffusive mixing efficiency ( $Q$ ), and  $\text{O}_3$  loss rates between 425K and 475K. A comparison between the observed and predicted correlation between  $\text{CH}_4$  and  $\text{O}_3$  within the vortex is also shown. The black line

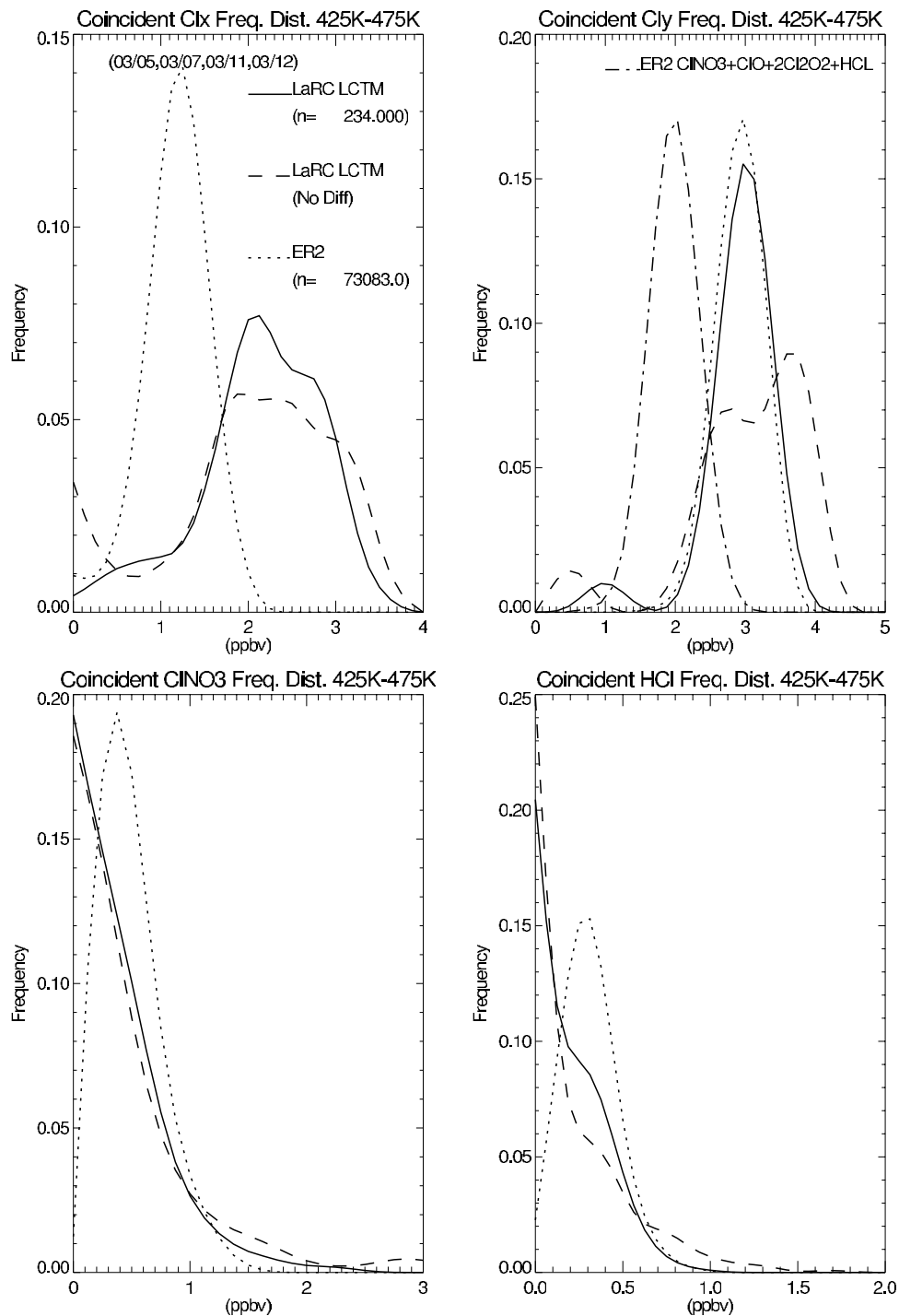


**Figure 10.** Frequency distributions of  $\text{Cl}_x$ ,  $\text{Cl}_y$ ,  $\text{ClNO}_3$ , and  $\text{HCl}$ , for vortex in situ measurements (dotted line) and coincident model trajectories between 425K and 475K taken on the 03/05, 03/07, 03/11, and 03/12 ER2 flights. Model frequency distributions are shown for simulations with (solid line) and without (dashed line) diffusive tendencies. The number in parenthesis below the line caption indicates the number of observations/trajectories used to construct the frequency distributions. The coincidence criteria were the same day,  $10^\circ$  longitude,  $5^\circ$  latitude, and 5K in potential temperature. The  $\text{Cl}_y$  frequency distribution (upper right panel) also shows the sum of the observed  $\text{ClNO}_3 + \text{ClO} + 2\text{Cl}_2\text{O}_2 + \text{HCl}$  (dash-dot line).

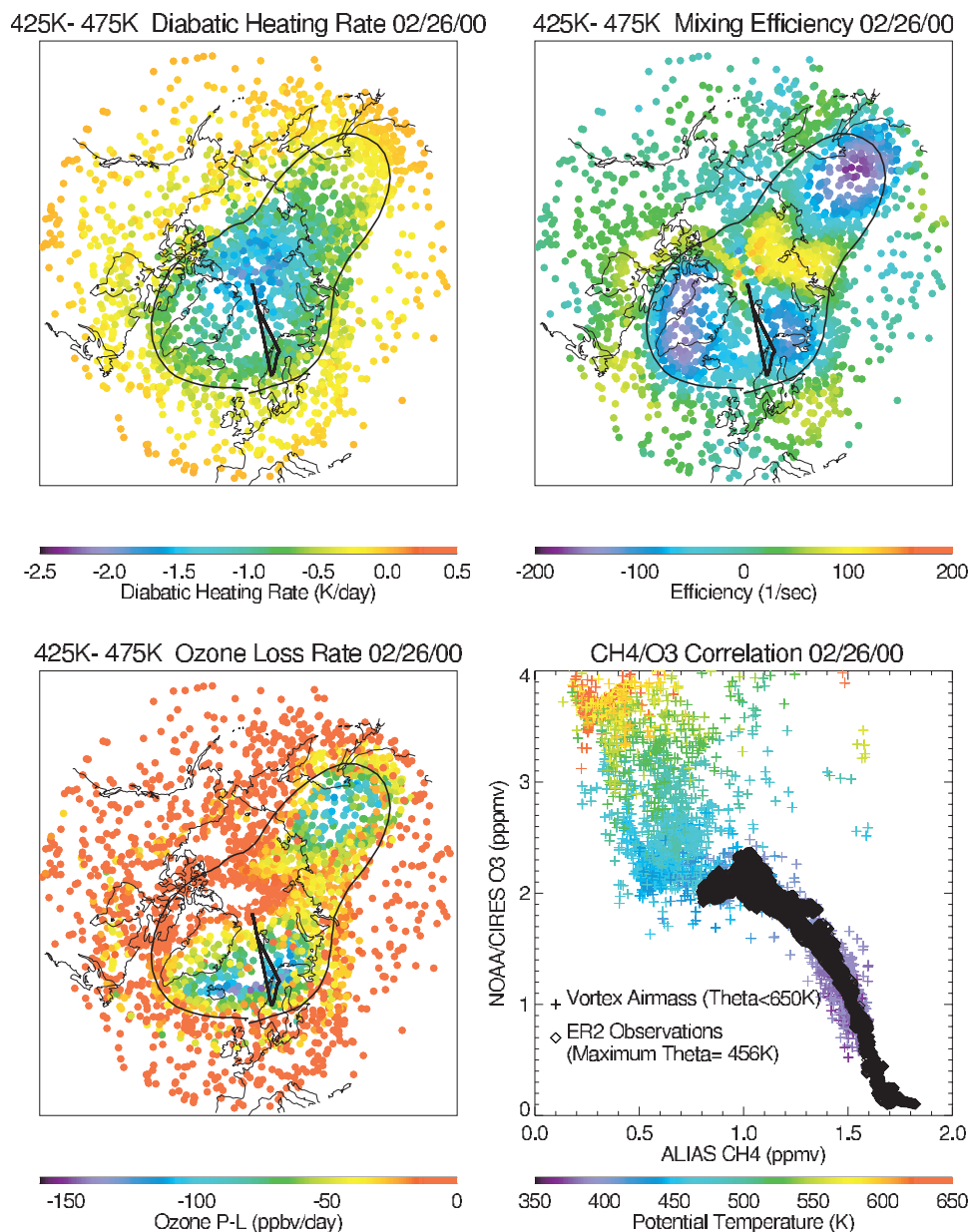


**Figure 11.** Synoptically mapped ensemble predictions of diabatic heating rates (K/day), diffusive mixing efficiency ( $Q$ ) ( $\text{sec}^{-1}$ ), and  $\text{O}_3$  loss rates between 425K and 475K on 26 February 2000 (02/26/00). The lower right panel shows a comparison between the observed (black triangles) and predicted (colored crosses) correlation between  $\text{CH}_4$  and  $\text{O}_3$  within the vortex. The black line in the synoptic maps indicates the kinematic edge of the Arctic vortex at 450K. The bold black line indicates the ER2 flight track.

in the synoptic maps indicates the kinematic edge of the Arctic vortex at 450K. The bold black line indicates the ER2 flight track.

[49] Diabatic heating (time rate of change in potential temperature following an air parcel) is the vertical velocity component in isentropic coordinates and negative diabatic heating implies descent of air through isentropic surfaces. The diabatic heating rates for the ensemble trajectories show considerable variability within the vortex with maximum diabatic cooling (descent) of approximately  $-2.0\text{K/day}$  occurring over the pole. The mixing efficiency shows even more variability within the vortex with three distinct lobes

of strongly negative  $Q$  (indicating a region of predominately rotational flow and no enhanced diffusive mixing) and a region between the lobes with strongly positive  $Q$  (indicating strong shear deformation and enhanced diffusive mixing). The shear zones and rotational lobes develop due to distortions in the Arctic vortex caused by midlatitude anti-cyclonic circulations to the north of Alaska and central Siberia. These midlatitude circulations are evident in the concave curvature of the kinematic edge and weakly negative ensemble  $Q$  in these regions.

[50] The region of maximum diabatic descent coincides with this enhanced mixing zone. This occurs since the

midlatitude disturbances which cause the vortex distortions also transport warm air poleward, leading to enhanced radiative cooling near the polar night jet core [Pierce *et al.*, 1993]. The largest enhancements in diffusive mixing tendencies (not shown) occur in the region of large  $Q$ , where both positive and negative tendencies are present. The episodes of enhanced diffusive mixing evident in Figures 5, 6, and 7 during February and March above 450K arise because of the coupling between the vertical constituent gradients, differential diabatic descent, and small-scale mixing processes. Strong diabatic descent over the pole introduces a population of trajectories that have descended from higher altitudes and have higher  $O_3$ ,  $NO_y$ , and  $Cl_y$  mixing ratios (and lower  $CH_4$  mixing ratios) than their neighboring trajectories, into the region of enhanced mixing. This population diffusively mixes with the neighboring trajectories with lower (higher) mixing ratios. Because the mean mixing ratio is conserved during each mixing event, the mean mixing ratios of the two populations are not affected. However, since trajectories encounter different populations at different altitudes as they descend within the vortex, the mean mixing ratio at a given level can be affected by diffusion. This process accounts for the shifts in the modeled frequency distributions when diffusive mixing is included in the simulations.

[51]  $O_3$  loss rates are generally in excess of 100 ppbv/day within the rotational lobes of the vortex at this time. These regions tend to be more isolated due to relatively weak winds and are at lower latitudes so that trajectories within the lobes have experienced longer periods of high daylight fractions than trajectories closer to the pole and within the shear zone (high  $Q$ ). Peak loss rates in the lobes over Greenland and Northern Scandinavia are as large as 140 ppbv/day. The air in the Scandinavian lobe was sampled by the ER2.

[52] The comparison between the observed and predicted  $CH_4/O_3$  correlation shows that the LaRC LCTM does a remarkable job in characterizing the compact nature of the  $CH_4/O_3$  correlation below 450K (the maximum potential temperature sampled by the ER2 on 26/02/00 was 456K). The measurements (black) overlay the model points with both showing  $O_3$  mixing ratios of approximately 2.0 ppmv for  $CH_4$  less than 1.0 ppmv. The model shows lower  $CH_4$  mixing ratios at 450K associated with the region of strong descent over the pole that was not sampled by the ER2. The lowest observed  $CH_4$  was encountered near 456K during the ER2's final climb before descent to Kiruna, Sweden. Consequently, the ER2 sampled air which was experiencing relatively high loss rates and was well removed from the region of strong diabatic descent and enhanced diffusive tendencies. Above 450K the model predicts a wide range in both  $O_3$  and  $CH_4$  for a given potential temperature bin.

#### 4.2. Case Study: 05/03/00

[53] The second case study considers the synoptic situation during the ER2 flight of 05/03/00 that occurred at the beginning of the large predicted  $O_3$  loss rates (see Figure 7). Figure 12 shows synoptically mapped ensemble predictions of condensed-phase  $HNO_3$  (NAT),  $Cl_x/Cl_y$ , and  $O_3$  net photochemical loss rates between 425K and 475K. A comparison between the observed and predicted correlation between  $CH_4$  and  $O_3$  within the vortex is also shown. Only

those trajectories with  $Cl_x/Cl_y$  ratios larger than 0.1 are shown to highlight the filament of processed air over the Maritime Provinces of Canada. Streamline contours are shown along with the NAT distribution to indicate the counter-clockwise circulation within the vortex.

[54] The model predicts a PSC encounter on the eastern leg of the ER2 flight track (shown in bold black), with condensed-phase  $HNO_3$  concentrations reaching 6.0 ppbv within the core. In situ  $NO_y$  and particle observations confirm the existence of this PSC. Photochemical losses are much more uniform than during the 02/26/00 case study since much of the vortex is outside of polar night. Photochemical loss rates range from near zero over Greenland (where the trajectories have just come over the pole and have spent time in polar night) to near 120 ppbv/day or approximately 5%/day along the eastern leg of the ER2 flight (in the region of the synoptic PSC). Chlorine activation is very high ( $Cl_x/Cl_y$  approaching 1.0) within the PSC, while just to the southeast of this region  $Cl_x/Cl_y$  ratios fall to near 0.6. This wide range of activation levels is reflected in the broad modeled  $Cl_x/Cl_y$  frequency distribution during this time period (Figure 9).

[55] The variation in activation levels arises as trajectories orbit around the vortex, pass through the synoptic scale NAT cloud on the Siberian side of the vortex where they become activated, and then slowly deactivate as they move along the warmer (near 215K) Canadian side of the vortex. Trajectories reach their lowest level of activation just prior to entering the western edge of the NAT cloud, which happens to be south of the ER2 flight track on this day. The rapid chlorine activation within the PSC most likely occurs via the heterogeneous reaction  $ClONO_2 + HCl \rightarrow Cl_2 + HNO_3$ , since there are ample chlorine reservoir species available just upstream. Highly activated trajectories are also found near the center of the vortex. These trajectories most likely passed through the synoptic PSC on some earlier day, or were activated due to heterogeneous reactions on sulfate aerosols (predicted vortex surface area densities at this time are near  $0.5 \mu m/cm^3$ ) and have remained activated as they stagnate in a region of relatively cold temperatures, limited sunlight, and weak circulation.

[56] There is a filament of vortex air in middle latitudes extending from central Siberia to the west coast of Greenland. Examination of daily maps from the simulation shows that this filament is a remnant of an earlier planetary wave breaking event that occurred on 29 February 1999, and resulted in significant export of processed air out of the vortex. The processed air rapidly mixes into the midlatitude background due to strong shear deformation on the equatorial flank of the polar night jet. However, the filament still shows  $O_3$  photochemical loss rates of up to 80 ppbv/day and moderately high  $Cl_x/Cl_y$  ratios (0.4–0.6), 5 days after it formed. Planetary wave breaking events were relatively infrequent during the 1999/2000 winter (in addition to the wave breaking on 29 February, there was an earlier event on 10 February at 450K). In general, the sharp demarcation in the photochemical characteristics of the ensemble trajectories (high chlorine activation, high  $O_3$  loss rates) is coincident with the kinematic edge of the Arctic vortex. The coincidence between the kinematic edge and the region of photochemical processing arises in spite of the fact that the photochemistry is largely independent of the edge defini-

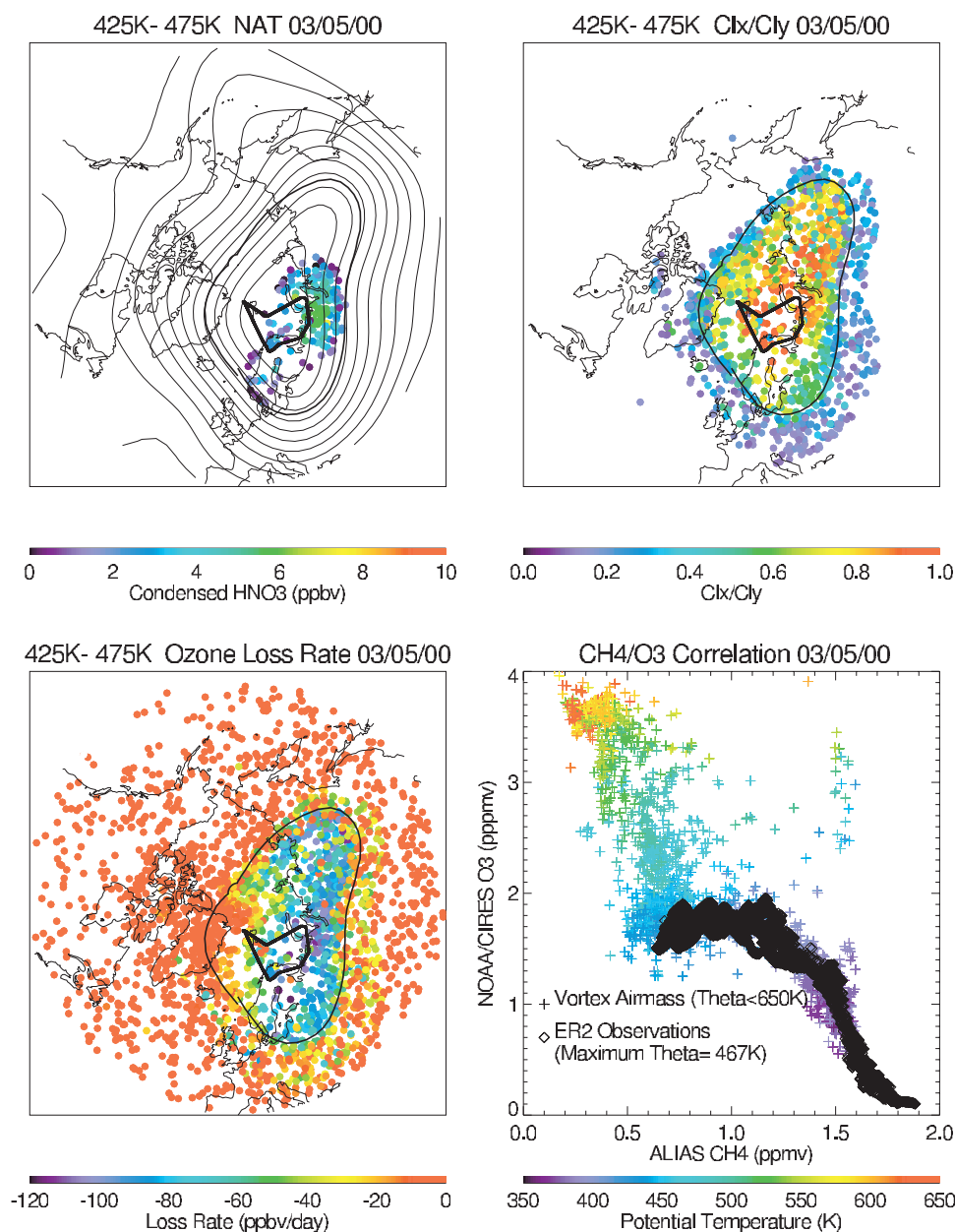


**Figure 12.** Synoptically mapped ensemble predictions of condensed-phase  $\text{HNO}_3$  (NAT) (ppbv),  $\text{Cl}_x/\text{Cl}_y$ , and  $\text{O}_3$  loss rates between 425K and 475K on 5 March 2000 (03/05/00). The lower right panel shows a comparison between the observed (black triangles) and predicted (colored crosses) correlation between  $\text{CH}_4$  and  $\text{O}_3$  within the vortex. The black line in the synoptic maps indicates the kinematic edge of the Arctic vortex at 450K. The bold black line indicates the ER2 flight track.

tion, highlighting the utility of the kinematic edge in defining the limit of chemical processing.

[57] The predicted correlation between  $\text{CH}_4$  and  $\text{O}_3$  once again does a very good job of reproducing the observed compact correlation at 450K where the measurements overlay the modeled  $\text{O}_3/\text{CH}_4$  correlation ( $\text{O}_3$  near 1.7 ppmv for  $\text{CH}_4$  mixing ratios below 1.0 ppmv). The model predicts a less compact correlation above 450K with a wide range of  $\text{CH}_4$  and  $\text{O}_3$  within relatively narrow potential temperature ranges. This variability is similar to the high variability found in early December (see Figure 2) and late February (see Figure 9) and suggests a relatively inhomogeneous

vortex just above the altitudes where the maximum  $\text{O}_3$  loss rates are found.

[58] This case study suggests that the disagreement between the observed and modeled chlorine activation (Figures 10 and 13) may arise due to the detailed timing of chlorine activation and de-activation as the air parcels orbit within the vortex. We cannot comment on the history of the air parcels observed by the ER2. But the slow deactivation predicted after trajectories encounter the synoptic scale PSC on 5 March arise because there is only about 0.01 ppbv of modeled  $\text{NO}_x$  available within the vortex during early March (consistent with the observed

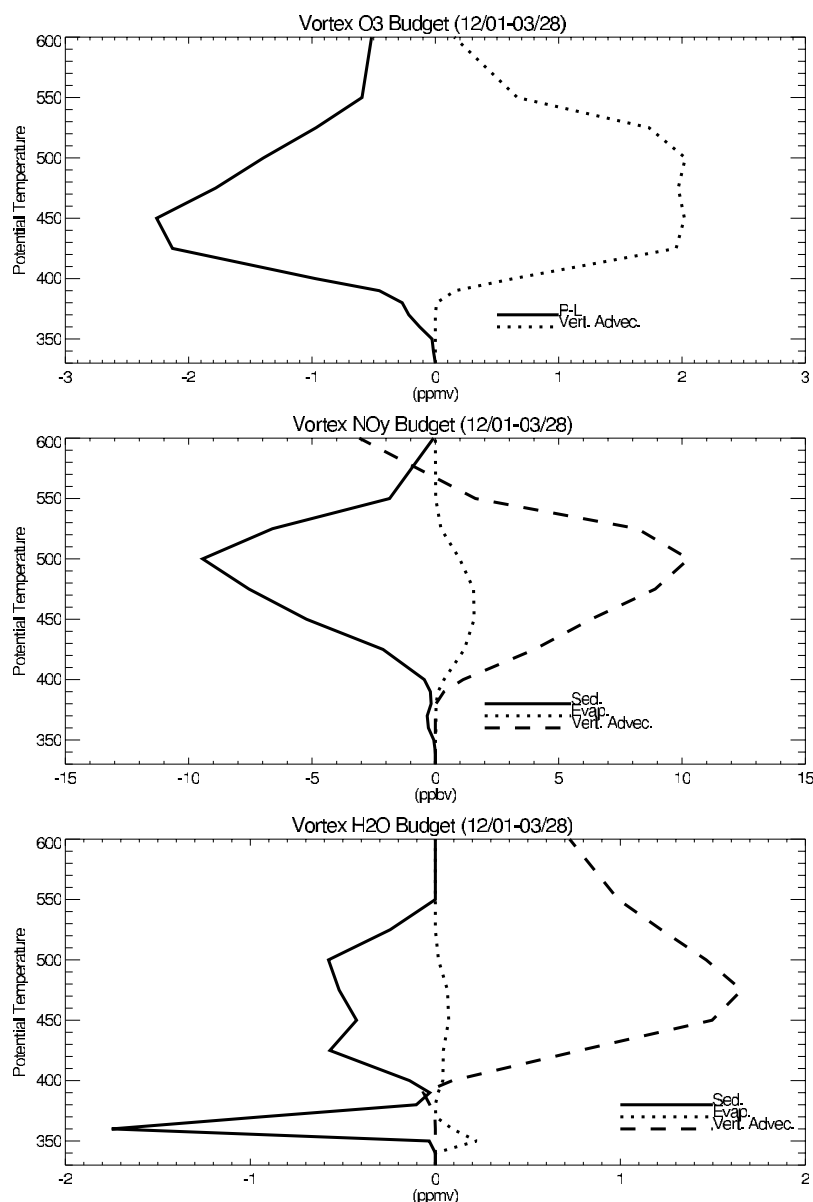


**Figure 13.** The vertical distribution of the accumulative sources/sinks in vortex  $O_3$ ,  $NO_y$ , and  $H_2O$  between 1 December 1999 (12/01) and 28 March 2000 (03/28) from the LaRC LCTM simulation is shown. The upper panel shows the accumulated effects of photochemical production-loss (P-L) and vertical advection on the vortex ensemble mean  $O_3$  distribution (ppbv). The middle panel shows the accumulated effects of Sedimentation (Sed.), evaporation (Evap.) and vertical advection on the vortex ensemble mean  $NO_y$  (ppbv). The lower panel shows the accumulated effects of Sedimentation (Sed.), evaporation (Evap.) and vertical advection on the vortex ensemble mean  $H_2O$  (ppmv).

$NO_x$  mixing ratios within the vortex), and many of the trajectories in the warmer Canadian side of the vortex are still in darkness. Interestingly, by 12 March, (near the end of the largest chlorine catalyzed ozone loss and just prior to the predicted rapid deactivation) the processes which maintain the model  $Cl_x/Cl_y$  ratios have changed. At this time, PSCs are no longer present but most vortex trajectories at 450K have temperatures near 200K, indicating that heterogeneous chlorine activation on sulfate aerosols is likely to play a significant role in extending the high chlorine activation out to mid-March in the model simulation. This shift in the physical processes responsible for maintaining the high

modeled  $Cl_x/Cl_y$  ratios over the period of one week illustrates the complex interactions between the temperature, sunlight, and heterogeneous processing history of vortex air parcels during early March. It is not surprising that we see significant differences in the rates of the predicted and observed chlorine deactivation given the complexity of the vortex evolution at this time.

## 5. Vortex Budgets

[59] Figure 13 shows budgets for vortex  $O_3$ ,  $NO_y$ , and  $H_2O$  in the LaRC LCTM simulation. The vortex budgets

were obtained by integrating the daily, ensemble mean tendencies during the period between 12/01 and 03/28. As shown earlier, the integrated photochemical  $O_3$  loss reaches a peak of 2.2 ppmv at 450K. The photochemical  $O_3$  losses are largely (but not completely) balanced by descent of high  $O_3$  mixing ratios from aloft, which is near 2.0 ppmv between 425K and 525K. Sedimentation results in a peak integrated  $NO_y$  loss of nearly 10 ppbv at 500K and evaporation results in approximately 2 ppbv increase in  $NO_y$  at 450K. The integrated change in  $NO_y$  due to vertical advection peaks at 500K with an accumulated increase of 10 ppbv. The model water vapor budget is dominated by vertical advection, which brings down 1.7 ppmv of  $H_2O$  at 475K. Sedimentation results in a peak integrated  $H_2O$  loss of 0.6 ppmv at 500K that is associated with the late December, early January ice PSCs. This dehydration is very close to that seen by in situ balloon measurements [Schiller *et al.*, 2002]. The 0.6 ppmv integrated  $H_2O$  loss at 420K is spurious, and is a result of rapid "rainout" (sedimentation at temperatures above ice frost point) of artificially high initial water vapor mixing ratios during the March PSC event. The high initial water vapor mixing ratios occurs because of uncertainties in the satellite water vapor retrievals when NAT aerosols are present. The net contribution due to  $H_2O$  evaporation is very small in the model. The vortex  $O_3$ ,  $NO_y$ , and  $H_2O$  budgets are nearly identical in the simulation without diffusion.

## 6. Impact of Mountain-Wave Activity

[60] Mountain waves (MWs) are small-scale gravity and inertial gravity waves generated by flow over topography that can propagate into the stratosphere under suitable conditions and leading to large temperature perturbations. If the temperatures within the MW drop below NAT or ice condensation points than orographic PSCs can form. Orographically induced PSCs were ubiquitous over the Norwegian Mountains during SOLVE. Carslaw *et al.* [1999] has shown that MWs can be a significant source of synoptic scale PSCs, extending several thousand kilometers downwind of the MW temperature anomalies.

[61] The LaRC LCTM simulation provides a unique opportunity to assess the impact of the MW activity on ozone loss within the Arctic vortex. The impact of temperature perturbations associated with MW activity on Arctic ozone loss is investigated by introducing daily three-dimensional temperature anomalies, predicted by the NRL Mountain Wave Forecast Model (MWFM 2.0) [Eckermann and Preusse, 1999], into the isentropic data base used for the LaRC LCTM simulations. MWFM 2.0 is a ray-based extension of the previous version of MWFM that considered a two-dimensional hydrostatic gravity waves. In the new version, wave group velocities are calculated using a rotating nonhydrostatic dispersion relation. Wave amplitudes are calculated using conservation of vertical flux of wave action, with rotational and nonhydrostatic terms retained. Wave breaking is accommodated through both convective and dynamical instability criteria. MWFM 2.0 uses meteorological model forecasts of wind and temperature to generate a forecast of mountain-wave activity. The key to producing this forecast is a detailed representation of global topography, which includes estimates of the

locations, widths, heights and orientations of nearly all mountain ridges on Earth with scales ranging from a hundred kilometers down to several kilometers. The MWFM ridge database is compiled from 5'x5' digital elevation data using objective techniques to identify significant features. This approach does a reasonable job of forecasting mountain-wave amplitudes in the upper troposphere and lower stratosphere [Bacmeister *et al.*, 1994] and was used to forecast mountain-wave effects operationally for flight planning during SOLVE (Eckermann *et al.*, unpublished manuscript, 2001).

[62] The MWFM provides grid point estimates of the mean amplitude and standard deviation of the small-scale temperature fluctuations using the Goddard 1x1 degree GEOS-2 Data Assimilation System (DAS) [Schubert *et al.*, 1993], winds and temperatures at standard pressure levels between 100 and 10 mb. The MW statistics are interpolated to the LaRC LCTM isentropic data base and then daily distributions of synthetic MW temperature perturbations are reconstructed. At each grid point the reconstruction first obtains a random sign of the MW temperature perturbation, which multiplies the MWFM mean amplitude, and then adds a temperature increment obtained from a random Gaussian distribution with a mean of zero and a standard deviation determined by the MWFM statistics. This reconstruction results in daily, gridded MW temperature perturbations that have the same three-dimensional distribution of means and standard deviations as the MWFM predictions, when averaged over a number of independent realizations (days). However, each large-scale gridbox has either a negative or positive MW temperature perturbation on a given day. In reality each trajectory would experience both positive and negative MW temperature perturbations as it transects the assimilated grid box. This means that the randomly signed MW temperatures will underestimate the true MW impact since 50% of the grid boxes with MW activity will have only positive temperature perturbations. To assess the bias introduced by the assumed MW temperature perturbation we considered two different MW scenarios, one with MW temperatures as defined above and one where the MW temperature perturbation is always negative. The randomly signed MW temperature perturbation provides a conservative lower bound on the actual impact and the negative MW temperature perturbation provides an absolute upper bound for assessing the impact of MW activity on Arctic  $O_3$  photochemistry.

[63] Figure 14 shows maps of the monthly mean amplitudes of the reconstructed MWFM temperatures at 450K, along with an indication of the percentage of time a given location was within the Arctic vortex during each month. Peak monthly mean MW amplitudes are near 3.0K, consequently MW perturbations will have the largest impact where the large-scale temperatures are already relatively close to the NAT frost point (i.e., within the Arctic vortex). Most of the strongest MW activity is associated with orography over North America, Tibet, and the Alps, which are generally located outside the Arctic vortex and within warmer air masses. However, regions of moderate MW activity are predicted within the Arctic vortex over the southeastern tip of Greenland, Iceland, Scandinavia, Siberia, and Alaska with monthly mean amplitudes of 1.0–1.5K. Of these regions, Scandinavia shows the largest monthly mean

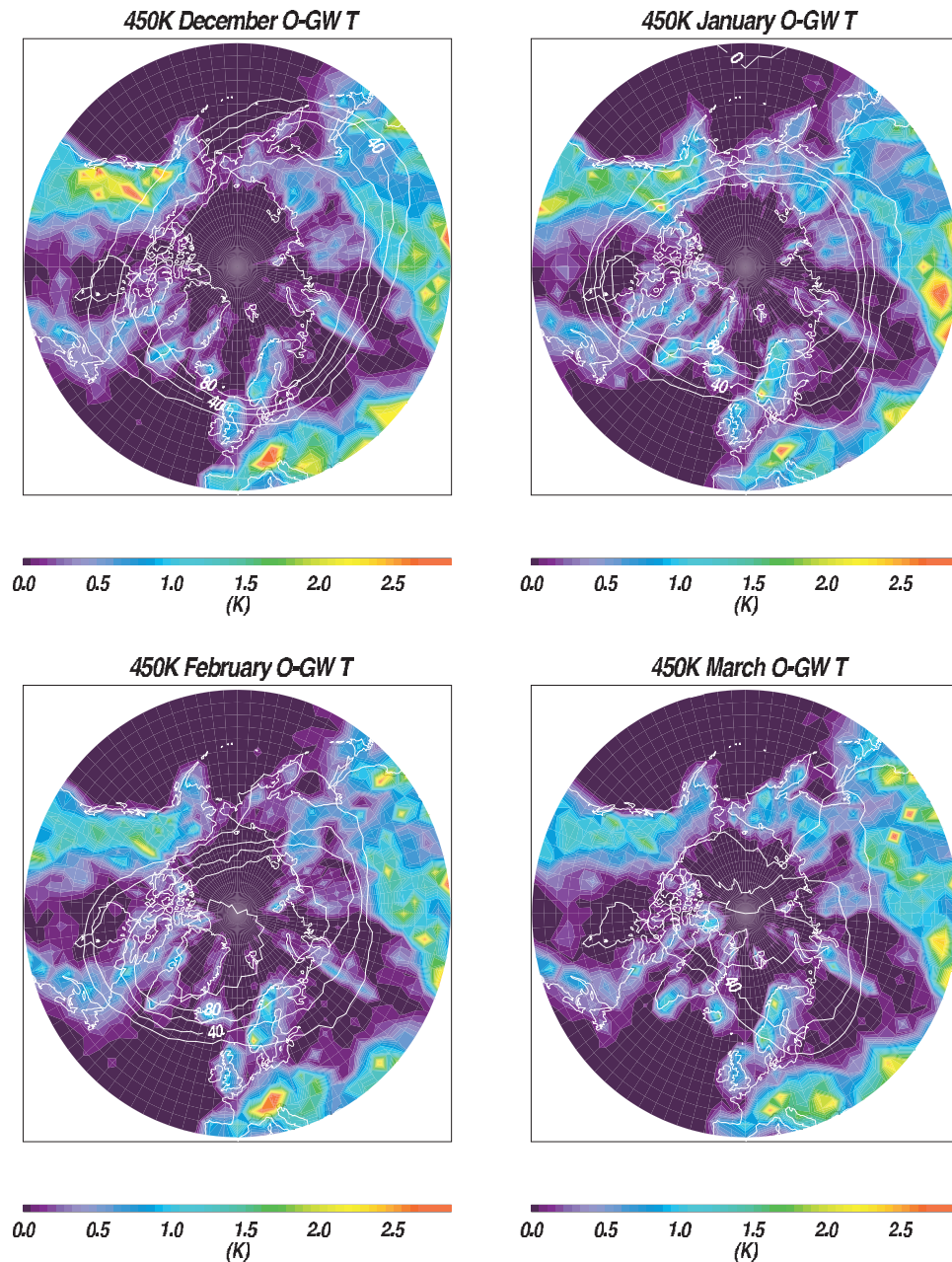


**Figure 14.** Maps of the monthly mean amplitudes of the reconstructed MWFM orographic gravity-wave (O-GW) temperatures (K) at 450K (shaded). Contours indicate the percentage of time a given location was within the Arctic vortex during each month.

predicted MW temperature perturbations and the most continuous exposure to the large-scale cold pool within the Arctic vortex. In fact, during each month, at least 40% of the Scandinavian MW activity was within the Arctic vortex at 450K during the 1999/2000 winter.

[64] The MW impact is determined by computing the differences between the accumulated vortex ensemble means for simulations with and without MW temperature perturbations. Figure 15 shows the impact of MW temperature perturbations on the vortex  $O_3$ ,  $NO_y$ , and  $H_2O$  budgets during the period from 1 December through 28 March 2000. The left panels show the results with the randomly signed MW perturbation and the right panels show the results with the negative MW perturbation. The random MW perturba-

tion shows small (less than 20 ppbv or 2%) increases in photochemical  $O_3$  loss, small (less than 0.15 ppbv or 2%) increases in  $NO_y$  sedimentation, and moderate (0.03 ppmv or 7%) increases in  $H_2O$  sedimentation between 450 and 550K. Smaller absolute changes in  $NO_y$  and  $H_2O$  evaporation occur below the potential temperature of the peak changes in sedimentation. The negative MW perturbations lead to a 100 ppbv (6%) change in the accumulated  $O_3$  photochemical loss within the vortex at 475K, a 0.8 ppbv (8%) change in the accumulated  $NO_y$  sedimentation at 500K, and a 0.15 ppmv (18%) change in the accumulated  $H_2O$  sedimentation at 450K. Consequently, the LaRC LCTM simulations indicate that the impact of MW on the accumulated photochemical  $O_3$  loss within the Arctic vortex

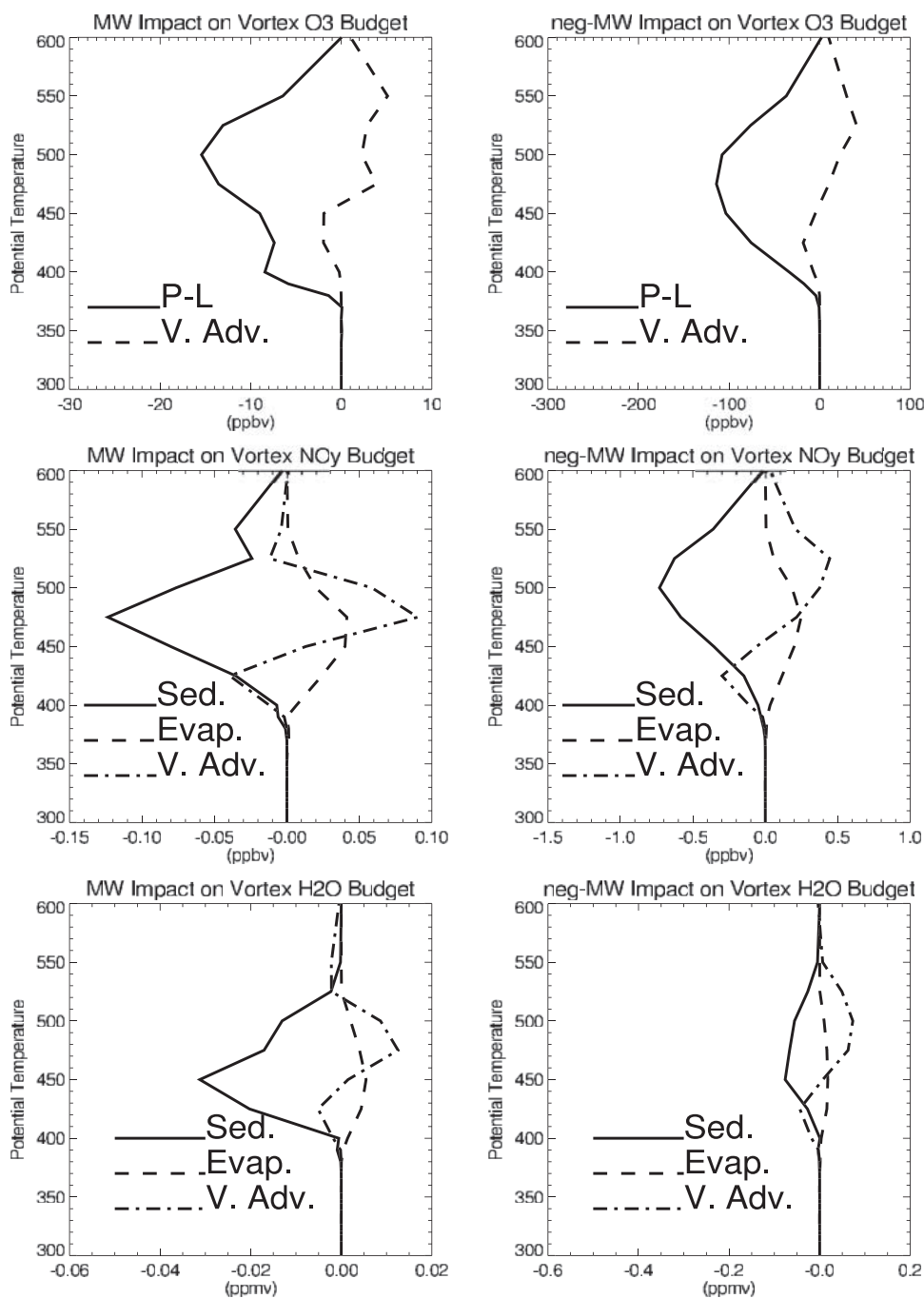


**Figure 15.** Impact of mountain-wave (MW) temperature perturbations on the vortex O<sub>3</sub>, NO<sub>y</sub>, and H<sub>2</sub>O budgets during the period from 1 December through 28 March 2000. The left panels show the results with the randomly signed MW perturbation and the right panels show the results with the negative MW perturbation.

during the 1999/2000 winter is a 2% to 6% increase in the accumulated loss, with similar impacts on the accumulated NO<sub>y</sub> sedimentation and 7% to 18% increases in the accumulated H<sub>2</sub>O sedimentation.

## 7. Conclusions

[65] The LaRC LCTM has been used in conjunction with HALOE and POAM III satellite observations to simulate

the large-scale photochemical evolution of the Arctic vortex during the 1999/2000 winter. Ensemble averaging of the vortex trajectories allows us to investigate the altitude-time distribution of the vortex evolution while synoptic mapping of the trajectories allows us to conduct focused case studies for comparisons with in situ and remote data obtained by ER2, DC8, and OMS Balloon payloads during SOLVE.

[66] The LaRC LCTM ensemble mean vortex predictions show significant denitrification occurring within the vortex

during late December 1999 and early January 2000 near 500K associated with extensive PSCs (primarily condensed-phase  $\text{HNO}_3$ , or NAT) within the vortex at these altitudes. Large-scale dehydration due to sedimentation of condensed  $\text{H}_2\text{O}$  occurred briefly during this same period and accounted for most of the modeled denitrification. The model's ability to predict the combined effects of diabatic descent, diffusive mixing and bulk PSC processes appears to be reasonable since the predictions of the extent of denitrification within the vortex are relatively good. However, the model tends to underestimate the denitrification for the majority of the vortex by approximately 10%, and does not show signatures of unprocessed air that are seen in the observations. The lack of unprocessed air in the model simulations is traced to overestimates in the diffusive mixing within the vortex.

[67] Predicted chlorine activation reaches over 80% of the available  $\text{Cl}_y$  during late January, declines slightly during February, and then increases again during March as renewed PSC activity occurs. The observed  $\text{Cl}_x/\text{Cl}_y$  ratio is near 0.4 during the March ER2 flights, significantly lower than predicted by the model. The synoptic case study on 05/03 shows that the spring time model chlorine activation biases arise due to subtle differences in the rates of chlorine activation on synoptic PSCs and down-stream de-activation as the trajectories orbit around the Arctic vortex. The high levels of activation predicted on 03/05 are maintained because of low  $\text{NO}_x$  and nearly continuous darkness, while mid-March activation is maintained via heterogeneous processing on sulfate aerosols. However, the exact extent of the overestimate is difficult to assess since there is an unaccounted for deficit in the observed chlorine species of approximately 33% relative to the ACATS total inorganic chlorine measurements. Increases in the observed  $\text{Cl}_x$  would reduce the observed deficit and would also reduce the model  $\text{Cl}_x/\text{Cl}_y$  bias, while increases in  $\text{ClONO}_2$  or  $\text{HCl}$  would also reduce the deficit but increase the model bias.

[68] The predicted net ensemble mean photochemical  $\text{O}_3$  loss reaches over 60 ppbv/day during the first two weeks of March. The predicted peak loss rate is in very good agreement with that inferred from the MATCH campaign ( $-61.6 \pm 4.8$  ppbv/day) during the same period, resulting in small differences in the accumulated  $\text{O}_3$  photochemical loss ( $-2.2$  ppmv predicted versus  $-2.7 \pm 0.24$  ppmv observed). The majority (55%) of the modeled photochemical loss is driven by  $\text{ClO}_x$  catalytic cycles with  $\text{BrO}_x$  cycles contributing the remaining 45%. Vertical advection nearly balances the photochemical  $\text{O}_3$  tendencies.

[69] The impact of mountain-wave temperature perturbations is investigated by blending the NRL MWFm mountain-wave temperature perturbations into the LaRC LCTM temperature fields. The results of sensitivity studies show that the impact of mountain-wave temperature perturbations on Arctic  $\text{O}_3$  depletion and  $\text{NO}_y$  denitrification range from 2–8% during the 1999/2000 winter. Larger MW impacts would be expected during winters without such extensive cold temperatures.

[70] This study highlights the combined effects of differential diabatic descent and horizontal diffusion on the distribution of trace gases within the vortex. Such coupling is unique to the Arctic because transient midlatitude dis-

turbances tend to distort the Arctic vortex more than its Southern Hemisphere counterpart, thus leading to lobe structures and shear zones with enhanced small-scale mixing efficiencies within the vortex. Maximum diabatic descent rates are often coincident with the enhanced mixing regions since the midlatitude disturbances which cause the vortex distortions also transport warm air poleward, leading to enhanced radiative cooling near the polar night jet core. The LaRC LCTM simulations show that diffusive mixing is necessary to accurately predict the distribution of chemical species within the Arctic vortex during the 1999/2000 winter. However, diffusive mixing does not significantly impact the ensemble mean  $\text{O}_3$  loss rates within the vortex.

[71] The results of the LaRC LCTM simulation during the 1999/2000 winter indicate that large-scale models with current chemistry can do a reasonable quantitative job in predicting the observed  $\text{O}_3$  loss and extent of denitrification in the Arctic vortex with bulk parameterizations of the PSC microphysics. However, significant disagreements remain. First, the modeled loss rates arise as a result of sustained periods of high chlorine activation during March, when the modeled chlorine activation is significantly higher than observed. Second, the extent of the observed denitrification is underestimated in the model simulation.

[72] **Acknowledgments.** Support for this work was provided by the NASA Atmospheric Chemistry, Modeling and Analysis Program (ACMAP).

## References

- Al-Saadi, J. A., R. B. Pierce, T. D. Fairlie, M. M. Kleb, R. S. Eckman, W. L. Grose, M. Natarajan, and J. R. Olson, Response of middle atmosphere chemistry and dynamics to volcanically elevated sulfate aerosol: Three-dimensional coupled model simulations, *J. Geophys. Res.*, 106, 27,255–27,275, 2002.
- Bacmeister, J. T., P. A. Newman, B. L. Gary, and K. R. Chan, An algorithm for forecasting mountain wave-related turbulence in the stratosphere, *Weather Forecasting*, 9, 241–253, 1994.
- Carslaw, K. S., B. P. Lu, and T. Peter, An analytical expression for the composition of aqueous  $\text{HNO}_3$ - $\text{H}_2\text{SO}_4$ - $\text{H}_2\text{O}$  stratospheric aerosols including gas phase removal of  $\text{HNO}_3$ , *Geophys. Res. Lett.*, 22, 1877–1880, 1995.
- Carslaw, K. S., T. Peter, J. T. Bacmeister, and S. D. Eckermann, Widespread solid particle formation by mountain waves in the Arctic stratosphere, *J. Geophys. Res.*, 104, 1827–1836, 1999.
- Carslaw, K. S., J. A. Kettleborough, M. J. Northway, S. Davies, R.-S. Gao, D. W. Fahey, D. Baumgardner, M. Chipperfield, and A. Kleinbohl, A vortex-scale simulation of the growth and sedimentation of large nitric acid hydrate particles, *J. Geophys. Res.*, 107(D20), 8300, doi:10.1029/2001JD000467, 2002.
- Chipperfield, M. P., Multiannual simulations with a three-dimensional chemical transport model, *J. Geophys. Res.*, 104, 1781–1805, 1999.
- Davies, S., et al., Modeling the effect of denitrification on Arctic ozone depletion during winter 1999/2000, *J. Geophys. Res.*, 107(D20), doi:10.1029/2001JD000445, in press, 2002.
- Drdla, K., M. R. Schoeberl, and E. V. Browell, Microphysical modeling of the 1999–2000 Arctic winter, 1, Polar stratospheric clouds, denitrification, and dehydration, *J. Geophys. Res.*, 107(D20), 8312, doi:10.1029/2001JD000782, 2002 [printed 108(D5), 2003].
- Eckermann, S. D., and P. Preusse, Global measurements of stratospheric mountain waves from Space, *Science*, 286, 1534–1537, 1999.
- Eckman, R. S., W. L. Grose, R. E. Turner, W. T. Blackshear, J. M. Russell III, L. Froidevaux, J. W. Waters, J. B. Kumer, and A. E. Roche, Stratospheric trace constituents simulated by a three-dimensional general circulation model: Comparison with UARS data, *J. Geophys. Res.*, 100, 13,951–13,966, 1995.
- Elkins, J. W., et al., Airborne gas chromatograph for in situ measurements of long-lived species in the upper troposphere and lower stratosphere, *Geophys. Res. Lett.*, 23, 347–350, 1996.
- Fahey, D. W., K. K. Kley, G. V. Ferry, L. R. Poole, J. C. Wilson, D. M. Murphy, M. Loewenstein, and K. R. Chan, In situ measurements of total

- reactive nitrogen, total water, and aerosol in polar stratospheric clouds in the Antarctic stratosphere, *J. Geophys. Res.*, *94*, 11,299–11,315, 1989.
- Fahey, D. W., et al., The detection of large HNO<sub>3</sub>-containing particles sampled in the Arctic stratosphere, *Science*, *291*, 1026–1031, 2001.
- Fairlie, T. D., R. B. Pierce, J. A. Al-Saadi, W. L. Grose, J. M. Russell III, M. H. Proffitt, and C. Webster, The contribution of mixing in Lagrangian photochemical predictions of polar ozone loss over the Arctic in summer 1997, *J. Geophys. Res.*, *104*, 26,597–26,609, 1999.
- Greenblatt, J. B., et al., Tracer-based determination of vortex descent in the 1999/2000 Arctic winter, *J. Geophys. Res.*, *107*(D20), 8279, doi:10.1029/2001JD000937, 2002.
- Herman, R. L., et al., Hydration, dehydration, and the total hydrogen budget of the 1999–2000 winter Arctic stratosphere, *J. Geophys. Res.*, *107*, doi:10.1029/2001JD001257, in press, 2002.
- Hofmann, D. J., and T. L. Deshler, Evidence from balloon measurements for chemical depletion of stratospheric ozone in the Arctic winter, *Nature*, *349*, 300–305, 1991.
- Kawa, S. R., R. M. Bevilacqua, J. J. Margitan, A. R. Douglass, M. R. Schoeberl, K. W. Hoppel, and B. Sen, Interaction between dynamics and chemistry of ozone in the setup phase of the Northern Hemisphere polar vortex, *J. Geophys. Res.*, *107*(D22), 8310, doi:10.1029/2001JD001527, 2002 [printed 108(D5), 2003].
- Lucke, R. L., et al., The Polar Ozone and Aerosol Measurement (POAM) III instrument and early validation results, *J. Geophys. Res.*, *104*, 18,757–18,799, 1999.
- Manney, G. L., and J. L. Sabutis, Development of the polar vortex in the 1999/2000 Arctic winter stratosphere, *Geophys. Res. Lett.*, *27*, 2589–2592, 2000.
- Manney, G. L., J. L. Sabutis, S. Pawson, M. L. Santee, B. Naujokat, R. Swinbank, M. E. Gelman, and W. Ebisuzaki, Lower stratospheric temperature differences between meteorological analyses in two cold Arctic winters and their impact on polar processing studies, *J. Geophys. Res.*, *107*, doi:10.1029/2001JD001149, in press, 2002.
- McKenna, D. S., et al., Calculation of ozone destruction during the 1988/1989 Arctic winter, *Geophys. Res. Lett.*, *17*, 553–556, 1990.
- Müller, R., P. J. Crutzen, J.-U. Grooss, C. Bruhl, J. M. Russell III, and A. F. Tuck, Chlorine activation and ozone depletion in the Arctic vortex: Observations by the Halogen Occultation Experiment on the Upper Atmosphere Research Satellite, *J. Geophys. Res.*, *101*, 12,531–12,554, 1996.
- Nash, E. R., P. A. Newman, J. E. Rosenfield, and M. R. Schoeberl, An objective determination of the polar vortex using Ertel's potential vorticity, *J. Geophys. Res.*, *101*, 9471–9478, 1996.
- Newman, P. A., J. F. Gleason, R. D. McPeters, and R. S. Stolarski, Anomalous low ozone over the Arctic, *Geophys. Res. Lett.*, *24*, 2689–2692, 1997.
- Northway, M. J., et al., An analysis of large HNO<sub>3</sub>-containing particles sampled in the Arctic stratosphere during the winter of 1999–2000, *J. Geophys. Res.*, *107*(D20), 8298, doi:10.1029/2001JD001079, 2002.
- Pierce, R. B., and T. D. Fairlie, Chaotic advection in the stratosphere: Implications for the dispersal of chemically perturbed air from the polar vortex, *J. Geophys. Res.*, *98*(D10), 18,589–18,595, 1993.
- Pierce, R. B., W. T. Blackshear, T. D. Fairlie, W. L. Grose, and R. E. Turner, The interaction of radiative and dynamical processes during a simulated sudden stratospheric warming, *J. Atmos. Sci.*, *50*, 3830–3851, 1993.
- Pierce, R. B., T. D. Fairlie, W. L. Grose, R. Swinbank, and A. O'Neill, Mixing processes within the polar night jet, *J. Atmos. Sci.*, *51*, 2957–2972, 1994.
- Pierce, R. B., J.-U. Grooss, W. L. Grose, J. M. Russell III, P. J. Crutzen, T. D. Fairlie, and G. Lingenfelter, Photochemical calculations along air mass trajectories during ASHOC/MAESA, *J. Geophys. Res.*, *102*, 13,153–13,167, 1996.
- Pierce, R. B., J. A. Al-Saadi, T. D. Fairlie, J. R. Olson, R. S. Eckman, W. L. Grose, G. S. Lingenfelter, and J. M. Russell III, Large-scale stratospheric ozone photochemistry and transport during the POLARIS campaign, *J. Geophys. Res.*, *104*, 26,525–26,545, 1999.
- Pierce, R. B., J. A. Al-Saadi, R. S. Eckman, T. D. Fairlie, W. L. Grose, M. M. Kleb, M. Natarajan, and J. R. Olson, Dynamical climatology of the NASA Langley Research Center Interactive Modeling Project for Atmospheric Chemistry and Transport (IMPACT) model, *J. Geophys. Res.*, *105*, 29,109–29,134, 2000.
- Proffitt, M. H., and R. J. McLaughlin, Fast-response dual-beam UV absorption ozone photometer suitable for use on stratospheric balloons, *Rev. Sci. Instrum.*, *54*, 1719–1728, 1983.
- Proffitt, M. H., K. Aikin, J. J. Margitan, M. Lowenstein, J. R. Podolske, A. Weaver, K. R. Chan, H. Fast, and J. W. Elkins, Ozone loss inside the northern polar vortex during the 1991–1992 winter, *Science*, *261*, 1150–1154, 1993.
- Randall, C. E., et al., Reconstruction of three-dimensional ozone fields using POAM III during SOLVE, *J. Geophys. Res.*, *107*(D20), doi:10.1029/2001JD000471, in press, 2002.
- Rex, M., et al., Chemical depletion of Arctic ozone in winter 1999/2000, *J. Geophys. Res.*, *107*(D20), 8276, doi:10.1029/2001JD000533, 2002.
- Russell, J. M., III, L. L. Gordley, J. H. Park, S. R. Drayson, W. D. Hesketh, R. J. Cicerone, A. F. Tuck, J. E. Frederick, J. E. Harries, and P. J. Crutzen, The Halogen Occultation Experiment, *J. Geophys. Res.*, *98*(D6), 10,777–10,798, 1993.
- Salawitch, R. J., et al., Loss of ozone in the Arctic vortex for the winter of 1989, *Geophys. Res. Lett.*, *17*, 561–564, 1990.
- Schiller, C., et al., Dehydration in the Arctic stratosphere during the SOLVE/THESEO 2000 campaigns, *J. Geophys. Res.*, *107*(D20), 8293, doi:10.1029/2001JD000463, 2002.
- Schubert, S. D., R. B. Rood, and J. Pfafndtner, An assimilated dataset for Earth science applications, *Bull. Am. Meteorol. Soc.*, *74*, 2331–2342, 1993.
- Schultz, A., et al., Arctic ozone loss in threshold conditions: MATCH observations in 1997/98 and 1998/99, *J. Geophys. Res.*, *106*, 7495–7503, 2001.
- Shine, K. P., The middle atmosphere in the absence of dynamical heat fluxes, *Q. J. R. Meteorol. Soc.*, *113*, 603–633, 1987.
- Solomon, S., Stratospheric ozone depletion: A review of concepts and history, *Rev. Geophys.*, *27*, 275–316, 1999.
- Swinbank, R., and A. O'Neill, A stratosphere-troposphere data assimilation system, *Mon. Weather Rev.*, *122*, 686–702, 1994.
- Toon, G. C., The JPL MkIV interferometer, *Opt. Photonics News*, *2*, 19–21, 1991.
- Toon, O. B., R. P. Turco, J. Jordan, J. Goodman, and G. Ferry, Physical processes in polar stratospheric ice clouds, *J. Geophys. Res.*, *94*, 11,359–11,380, 1989.
- Webster, C. R., R. D. May, C. A. Trimble, R. G. Chave, and J. Kendall, Aircraft (ER-2) Laser Infrared Absorption Spectrometer (ALIAS) for in-situ stratospheric measurements of HCl, N<sub>2</sub>O, CH<sub>4</sub>, NO<sub>2</sub>, and HNO<sub>3</sub>, *Appl. Opt.*, *33*, 454–472, 1994.
- Wennberg, P. O., et al., Removal of stratospheric O<sub>3</sub> by radicals: In situ measurements of OH, HO<sub>2</sub>, NO, NO<sub>2</sub>, ClO, and BrO, *Science*, *266*, 398–404, 1994.
- J. Al-Saadi, T. D. Fairlie, W. L. Grose, M. Natarajan, and R. B. Pierce, NASA Langley Research Center, Hampton, VA 23681, USA. (r.b.pierce@larc.nasa.gov)
- R. Bevilacqua, Code 7220, Remote Sensing Division, Naval Research Laboratory, 4555 Overlook Avenue, SW, Washington, DC 20032, USA. (bevilacq@poamb.nrl.navy.mil)
- S. D. Eckermann, Code 7641, E. O. Hulburt Center for Space Research, Naval Research Laboratory, 4555 Overlook Avenue, SW, Washington, DC 20032, USA. (eckerman@map.nrl.navy.mil)
- J. Elkins, R/CMDL1, Climate Monitoring and Diagnostics Laboratory, National Oceanic and Atmospheric Administration, 325 Broadway, Boulder, CO 80305, USA. (jelkins@cmdl.noaa.gov)
- D. Fahey, P. Popp, and E. Richard, R/AL6, Aeronomy Laboratory, National Oceanic and Atmospheric Administration, 325 Broadway, Boulder, CO 80305, USA. (fahey@al.noaa.gov)
- V. L. Harvey, Science Applications International Corporation, MS 401B, Langley Research Center, National Aeronautics and Space Administration, Hampton, VA 23665, USA. (v.l.harvey@larc.nasa.gov)
- J. M. Russell III, Center for Atmospheric Sciences, 23 Tyler Street, Hampton University, P.O. Box 6075, Hampton, VA 23669, USA. (james.russell@hamptonu.edu)
- R. Stimpfle, Anderson Group/CCB, Department of Chemistry, Harvard University, 12 Oxford Street, Cambridge, MA 02138, USA. (stimpfle@huarp.harvard.edu)
- G. C. Toon, Mail Stop 183–601, Jet Propulsion Laboratory, National Aeronautics and Space Administration, 4800 Oak Grove Drive, Pasadena, CA 91109, USA. (toon@mark4sun.jpl.nasa.gov)
- C. R. Webster, Mail Code 183–401, Jet Propulsion Laboratory, National Aeronautics and Space Administration, 4800 Oak Grove Drive, Pasadena, CA 91109, USA. (chris.r.webster@jpl.nasa.gov)